University of Groningen

The incidence of AGN in galaxies with different stellar population ages

Ni, Q.; Aird, J.; Merloni, A.; Birchall, K. L.; Buchner, J.; Salvato, M.; Yang, G.

Published in:
Monthly Notices of the Royal Astronomical Society

DOI:
10.1093/mnras/stad2070

IMPORTANT NOTE: You are advised to consult the publisher's version (publisher's PDF) if you wish to cite from it. Please check the document version below.

Document Version
Publisher's PDF, also known as Version of record

Publication date:
2023

Link to publication in University of Groningen/UMCG research database

Citation for published version (APA):
Ni, Q., Aird, J., Merloni, A., Birchall, K. L., Buchner, J., Salvato, M., & Yang, G. (2023). The incidence of AGN in galaxies with different stellar population ages. *Monthly Notices of the Royal Astronomical Society*, *524*(3), 4778-4800. https://doi.org/10.1093/mnras/stad2070

Copyright
Other than for strictly personal use, it is not permitted to download or to forward/distribute the text or part of it without the consent of the author(s) and/or copyright holder(s), unless the work is under an open content license (like Creative Commons).

The publication may also be distributed here under the terms of Article 25fa of the Dutch Copyright Act, indicated by the "Taverne" license. More information can be found on the University of Groningen website: https://www.rug.nl/library/open-access/self-archiving-pure/taverne-amendment.

Take-down policy
If you believe that this document breaches copyright please contact us providing details, and we will remove access to the work immediately and investigate your claim.

Downloaded from the University of Groningen/UMCG research database (Pure): http://www.rug.nl/research/portal. For technical reasons the number of authors shown on this cover page is limited to 10 maximum.

Download date: 31-10-2023

Monthly Notices of the ROYAL ASTRONOMICAL SOCIETY

MNRAS **524,** 4778–4800 (2023) https://doi.org/10.1093/mnras/stad2070
Advance Access publication 2023 July 13

The incidence of AGN in galaxies with different stellar population ages

Q. Ni,[1,2★] J. Aird,[1] A. Merloni,[2] K. L. Birchall,[3] J. Buchner,[2] M. Salvato[2] and G. Yang[4,5]

[1] *Institute for Astronomy, University of Edinburgh, Royal Observatory, Edinburgh EH9 3HJ, UK*
[2] *Max-Planck-Institut für extraterrestrische Physik (MPE), Gießenbachstraße 1, D-85748 Garching bei München, Germany*
[3] *School of Physics & Astronomy, University of Leicester, University Road, Leicester LE1 7RH, UK*
[4] *Kapteyn Astronomical Institute, University of Groningen, PO Box 800, 9700 AV Groningen, the Netherlands*
[5] *SRON Netherlands Institute for Space Research, Postbus 800, 9700 AV Groningen, the Netherlands*

Accepted 2023 June 25. Received 2023 May 30; in original form 2023 March 24

ABSTRACT

It has been argued that recycled gas from stellar mass loss in galaxies might serve as an important fuelling source for black holes (BHs) in their centres. Utilizing spectroscopic samples of galaxies from the Sloan Digital Sky Survey (SDSS) at $z = 0$–0.35 and the Large Early Galaxy Astrophysics Census (LEGA-C) survey at $z = 0.6$–1 that have X-ray coverage from *XMM–Newton* or *Chandra*, we test this stellar mass loss fuelling scenario by investigating how AGN activity and BH growth vary with the break strength at 4000 Å, D_n4000 (which is closely related to the age of stellar populations), as younger galaxies are considered to have higher stellar mass loss rates. We found that when controlling for host-galaxy properties, the fraction of log $L_X/M_\star > 32$ (which roughly corresponds to Eddington ratios $\gtrsim 1$ per cent) AGN and sample-averaged black hole accretion rate ($\overline{\mathrm{BHAR}}$) decrease with D_n4000 among $D_n4000 \lesssim 1.9$ galaxies, suggesting a higher level of AGN activity among younger galaxies, which supports the stellar mass loss fuelling scenario. For the oldest and most massive galaxies at $z = 0$–0.35, this decreasing trend is not present anymore. We found that, among these most massive galaxies at low redshift, the fraction of low specific-accretion-rate ($31 <$ log $L_X/M_\star < 32$) AGNs increases with D_n4000, which may be associated with additional fuelling from hot halo gas and/or enhanced accretion capability.

Key words: galaxies: active – galaxies: evolution – galaxies: nuclei – X-rays: galaxies.

1 INTRODUCTION

In the past decades, the understanding of how galaxies evolve over cosmic history has progressed rapidly as a result of accumulating data from various imaging and spectroscopic surveys (e.g. Kauffmann et al. 2003; Faber et al. 2007; Madau & Dickinson 2014; van der Wel et al. 2014; Barro et al. 2017; Wu et al. 2018). Galaxies appear to follow a range of evolutionary pathways, whereby their stellar populations and gas properties change over time, although the physical processes that drive these transformations are still unclear. While supermassive black holes (BHs) only occupy a small space in the galaxy centres, they are thought to play an important role in galaxy evolution. As the mass of BHs is found to be tightly correlated with the mass of their host bulges (e.g. Magorrian et al. 1998; Marconi & Hunt 2003; Kormendy & Ho 2013; McConnell & Ma 2013), BHs appear to coevolve with their host galaxies. While we know that central supermassive BHs grow primarily by accreting gas and can be seen as Active Galactic Nuclei (AGNs), the exact feeding mechanism of BHs remains unclear. It is important to investigate what drives the growth of BHs, which will ultimately reveal the physical mechanisms behind the potential coevolution scenario.

It has been found that BH accretion rate tracks the star formation rate over cosmic history, suggesting cold gas supply as a common fuel for both the galaxy and the BH (e.g. Aird et al. 2010; Kormendy & Ho 2013). However, the noticeable fraction of AGNs in quiescent galaxies (given their low level of star formation activity and thus inferred low level of global cold gas content) indicates that additional mechanisms may fuel the growth of central BHs after quenching (e.g. Kocevski et al. 2017; Wang et al. 2017; Aird, Coil & Georgakakis 2019; Aird, Coil & Kocevski 2022). Among galaxies where the cold gas supply is not sufficient, stellar mass loss may provide an important, additional source of fuel for accretion onto the BH (e.g. Hopkins & Hernquist 2006; Ciotti & Ostriker 2007; Kauffmann & Heckman 2009). In this scenario, as galaxies with younger stellar populations have stronger stellar winds and higher mass loss rates that provide more fuel for the central BHs, BH growth is expected to vary among galaxies with different ages of stellar populations. Through characterizing the AGN activity across the lifecycle of galaxies, we can investigate the role of stellar mass loss in fuelling BHs.

As spectra can provide direct information about the age of stellar populations through features such as the break strength at 4000 Å, D_n4000, large samples of galaxies and AGNs with spectroscopic coverage are needed to investigate the potential fuelling through stellar mass loss. In the local universe, the Sloan Digital Sky Survey (SDSS) provides a large legacy sample of galaxies (e.g. Strauss et al. 2002), and the X-ray information provided by serendipitous catalogues from accumulating X-ray observations over the entire sky (e.g. Evans et al. 2010; Webb et al. 2020) provides opportunities to effectively identify AGNs among this large galaxy sample (e.g. Brandt & Alexander 2015; Brandt & Yang 2021). More recently, deep spectroscopic surveys (e.g. van der Wel et al. 2016; McLure et al. 2018) have started to help build representative samples of galaxies at intermediate reshifts. When deep X-ray coverage is available,

★ E-mail: qingling1001@gmail.com

© 2023 The Author(s)
Published by Oxford University Press on behalf of Royal Astronomical Society

Downloaded from https://academic.oup.com/mnras/article/524/3/4778/7224006 by Rijksuniversiteit Groningen user on 26 September 2023

these surveys can also be effectively utilized to study the incidence of AGNs in galaxies with different stellar population ages (e.g. Silverman et al. 2009; Mountrichas et al. 2022; Georgantopoulos et al. 2023).

In this paper, we use samples of galaxies from SDSS and the Large Early Galaxy Census (LEGA-C; e.g. van der Wel et al. 2016) survey to investigate how AGN activity and BH growth vary with D_n4000 across the galaxy lifecycle at $z = 0 - 0.35$ and $z = 0.6 - 1$. We also test whether AGN activity and BH growth vary with D_n4000 when other galaxy properties are controlled, thus revealing whether the age of stellar populations has a fundamental influence on AGN activity/BH growth.

The paper is structured as follows. In Section 2, we describe the sample construction process. In Section 3, we detail the analysis results and discuss what they imply in Section 4. The conclusions are presented in Section 5. Throughout this paper, stellar masses ($M_\star$) are given in units of $M_\odot$; star formation rates (SFRs) and sample-averaged black hole accretion rates ($\overline{\rm BHAR}$) are given in units of $M_\odot$ yr^{-1}. L_X represents X-ray luminosity at rest-frame 2–10 keV in units of erg s^{-1}. Quoted uncertainties are at the 1σ (68 per cent) confidence level. A cosmology with $H_0 = 70$ km s^{-1} Mpc^{-1}, $\Omega_M = 0.3$, and $\Omega_\Lambda = 0.7$ is assumed.

2 DATA AND SAMPLE SELECTION

Two samples of X-ray AGNs with spectroscopic coverage are utilized in this study: one sample includes SDSS galaxies with *XMM–Newton* coverage (see Section 2.1); one sample includes LEGA-C galaxies with *Chandra* coverage in the COSMOS field (see Section 2.2). In Section 2.4, we discussed how the AGN fraction and $\overline{\rm BHAR}$ are estimated.

2.1 Constructing a sample of SDSS galaxies with *XMM–Newton* coverage

2.1.1 *Selecting galaxies in MPA-JHU catalogue with* XMM–Newton *coverage*

The SDSS galaxy/AGN sample utilized in the study is built upon the MPA-JHU value-added catalogue.[1] The MPA-JHU catalogue provides galaxy property measurements for SDSS DR8 spectra classified by the pipeline as a galaxy (SPECTROTYPE = GALAXY), including D_n4000, $M_\star$, and SFR used in this study. We only consider objects observed as the prime targets in the SDSS Legacy Survey Main Galaxy Sample in this study.[2]

D_n4000 in the MPA-JHU catalogue is measured according to the Balogh et al. (1999) definition, as the ratio of the flux in the 4000–4100 Å continuum to that in the 3850–3950 Å continuum. $M_\star$ values are measured following model grids based on SDSS photometry, as described in Kauffmann et al. (2003). SFR values are measured by combining emission line measurements from Brinchmann et al. (2004) with aperture corrections as described in Salim et al. (2007). $M_\star$ and SFR values in the MPA-JHU catalogue are largely consistent with those derived from Galex-SDSS-WISE SED fitting (e.g. Salim et al. 2016), and have been widely adopted.

We use the RapidXMM data base (Ruiz et al. 2022) to select galaxies in MPA-JHU catalogue within *XMM–Newton* coverage. RapidXMM provides *XMM–Newton* aperture photometry as well as upper limits within HEALPix cells of size ≈ 3 arcsec. As the 4XMM-DR11 catalogue (Webb et al. 2020) is utilized to match galaxies with their *XMM–Newton* counterparts for X-ray AGN identification (see Section 2.1.2), we limit our sample to SDSS galaxies with *XMM–Newton* point observations made before 2020 December 17.

2.1.2 *Matching selected galaxies with* XMM–Newton *counterparts*

The 4XMM-DR11 catalogue used in this study to provide X-ray counterparts to SDSS galaxies contains sources drawn from a total of 12 210 *XMM–Newton* observations made between 2000 February 1 and 2020 December 17, including ∼ 600 000 unique X-ray sources over ≈ 1239 deg^2.

As SDSS galaxies in the MPA-JHU catalogue are a subset of SDSS objects, we first match X-ray sources in the 4XMM DR11 catalogue with SDSS DR8 (Adelman-McCarthy et al. 2011) and catWISE (Marocco et al. 2021) catalogues, and use the obtained optical/NIR counterparts positions to further match with MPA-JHU galaxies. When we perform the source matching, we only consider 4XMM sources that are within 30 arcmin of MPA-JHU sources, thus restricting to 4XMM sources that lie within the footprint of the MPA-JHU catalogue. The input SDSS and WISE catalogues only include objects within 1 arcmin of 4XMM sources, to save computation time. Following the method in Ni et al. (2021a), we use NWAY (Salvato et al. 2018) to perform the source matching, with priors obtained from sources reported in the *Chandra* Source Catalogue (CSC) 2.0 (Evans et al. 2010) that are matched to the 4XMM sources within the 95 per cent uncertainties (as *Chandra* detections have better positional accuracy than *XMM–Newton* detections). Utilizing the SDSS and WISE sources that are matched to these *Chandra* sources within 5″, we obtain priors in the WISE W1+W2 versus W1−W2 colour space and in the *i*-band magnitude space. With these priors, we match 4XMM sources to their optical/NIR counterparts. Matched primary counterparts with $p_{\rm any} > 0.1$ and $p_{\rm i} > 0.1$ are adopted as reliable matches. We then match MPA-JHU galaxies to these obtained optical/NIR positions of 4XMM sources with a 1″ matching radius. To assess the matching accuracy, we use the 4XMM sources that have *Chandra* counterparts, and compare the level of agreement between matched MPA-JHU sources when either 4XMM or CSC position is used. The matched MPA-JHU counterparts of 4XMM sources have a ≈96 per cent agreement with those of CSC sources.

2.2 LEGA-C galaxies in the COSMOS field

To extend the redshift range probed in this study, we also include galaxies/AGNs in the LEGA-C Data Release 3 (van der Wel et al. 2021) which have *Chandra* X-ray coverage from the COSMOS-Legacy survey (Civano et al. 2016).[3] We only utilize sources in the LEGA-C catalogue with PRIMARY = 1, FLAG_MORPH = 0, and FLAG_SPEC < 2; D_n4000 values are available for 2129 of these sources, measured according to the Balogh et al. (1999) definition as well. We also examine the spectra visually and remove spectra with broad emission lines from the sample. We cross-match these sources to the photometric sample of galaxies in the COSMOS field in Ni et al. (2021b), which provides $M_\star$ and SFR measurements for sources within both the COSMOS and UltraVISTA regions utilizing photometric data in 38 bands (including 24 broad bands) from NUV to FIR (Laigle et al. 2016) and the SED-fitting code `CIGALE` (e.g. Boquien et al. 2019; Yang et al. 2020). X-ray counterparts from

[1] http://www.mpa-garching.mpg.de/SDSS/DR7/

[2] Galaxies in the SDSS Legacy Survey are observed with 3″-diameter fibers.

[3] Galaxies in the LEGA-C survey are observed with 1″ × 8″ slits.

Downloaded from https://academic.oup.com/mnras/article/524/3/4778/7224006 by Rijksuniversiteit Groningen user on 26 September 2023

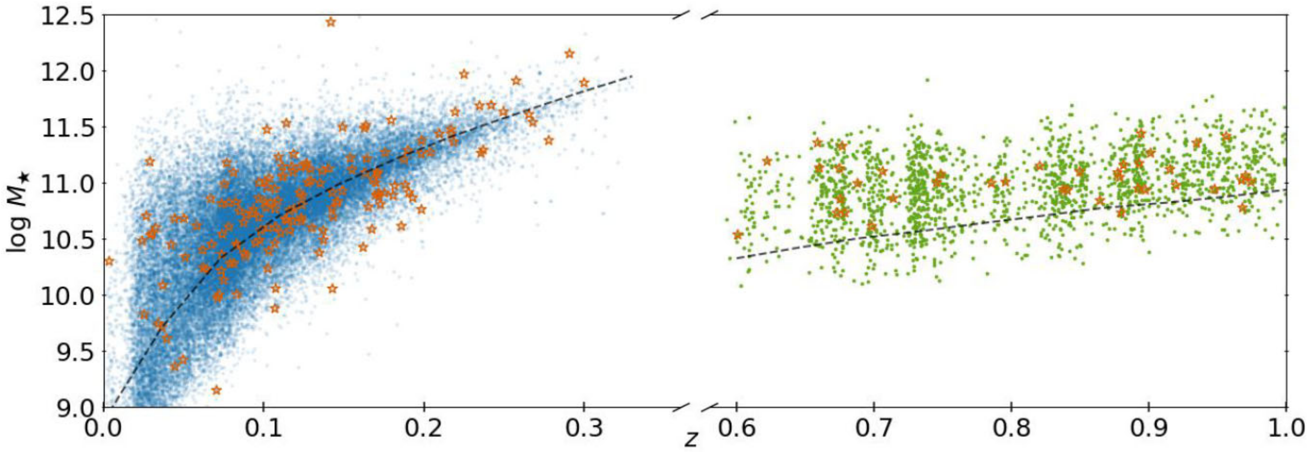

Figure 1. $M_\star$ as a function of z for SDSS main sample galaxies in the MPA-JHU catalogue with *XMM–Newton* coverage (blue dots) and galaxies included the LEGA-C survey (green dots). X-ray AGNs with log $L_X/M_\star > 32$ are marked as orange stars. The dashed curve indicates the 90 per cent $M_\star$ completeness limit as a function of redshift.

Chandra are also matched for this photometric sample of galaxies in Ni et al. (2021b). The detailed process to obtain $M_\star$ and SFR measurements can be seen in Section 2.1 of Ni et al. (2021b). An AGN component is included in the SED fitting, in addition to the galaxy component. As discussed in Ni et al. (2021b), adding the X-ray information or not during the SED fitting does not significantly affect the Bayesian $M_\star$ and SFR measurements. Uncertainties of the $M_\star$ and SFR values obtained are also discussed in Section 2.1 and appendix A of Ni et al. (2021b). We note that $M_\star$ measurements are generally robust when comparing results from different SED fitting methods, with a scatter of $\approx$ 0.1 dex; the scatter of SFR measurements can be up to $\approx$ 0.4 dex. This finally provides a sample of 1792 galaxies in the COSMOS field.

2.3 Sample properties

In Fig. 1, we present the $M_\star$ versus z distributions for the selected SDSS galaxies and LEGA-C galaxies. For SDSS galaxies with *XMM–Newton* coverage, we plot the 90 per cent $M_\star$ completeness curve of galaxies in the SDSS main galaxy sample. The limiting $M_\star$ is derived following Section 3.2 of Ilbert et al. (2013) given the r-band Petrosian magnitude limit of 17.77 of the SDSS main galaxy sample (Strauss et al. 2002). In our study, we only utilize SDSS galaxies above this mass-completeness curve, and we refer to this galaxy sample as the 4XMM sample throughout the remainder of this work. The LEGA-C primary targets are drawn from a K_s-band selected parent sample; these targets are representative of the parent sample when taking into account the selection correction factor SCOR provided in the LEGA-C catalogue (see Appendix A of van der Wel et al. 2021 for details). This selection correction factor is utilized in our analyses to weight each galaxy, although we find that excluding this factor does not impact our results materially (see Section 3.1 for details). The 90 per cent $M_\star$ completeness curve for the parent sample (which has a redshift-dependent K_s-band limiting magnitude of $20.7 - 7.5 \times \log((1 + z)/1.8)$) is shown on the plot. In our study, we only utilize LEGA-C galaxies above this mass-completeness curve of the parent sample, and we refer to this galaxy sample as the COSMOS sample throughout the remainder of this work. We carry out our studies with mass-complete samples to avoid any potential bias associated with an incomplete characterization of galaxy populations. In Table 1, we present the properties of the 4XMM sample and the COSMOS sample. In Figs 2 and 3, we present how galaxies/AGNs in our samples distribute on the SFR versus $M_\star$ plane, SFR versus D_n4000 plane, and D_n4000 versus $M_\star$ plane; we also present the D_n4000 distribution of galaxies/AGNs. In Appendix A, we show that the contamination from AGN emission to D_n4000 measurements is small for AGNs in our sample, and will not materially affect our results.

Table 1. Summary of sample properties. (1) Name of the sample. (2) Redshift range of the sample. (3) $M_\star$ range of the sample. (4) Number of galaxies in the sample. (5) Number of log $L_X/M_\star > 32$ AGNs.

Sample name (1)	Redshift range (2)	Mass range (3)	Number of galaxies (4)	Number of AGNs (5)
4XMM	0–0.35	log$M_\star > 9$	22 576	89
COSMOS	0.6–1.0	log$M_\star > 10$	1496	38

2.4 Obtaining AGN fraction and sample-averaged BH accretion rate

The AGN fraction is defined in terms of $L_X/M_\star$ (as advocated by Bongiorno et al. 2016; Aird, Coil & Georgakakis 2018, 2019; Aird et al. 2022; Birchall et al. 2022), which measures the rate of BH growth relative to the stellar mass of the host galaxy (i.e. the 'specific BH accretion rate') and thus accounts for the overall stellar-mass-selection bias whereby weakly accreting AGN in more massive galaxies have a higher L_X and are thus easier to detect (see Aird et al. 2012). AGN fractions throughout this work, unless otherwise stated, refer to objects with log $L_X/M_\star \geq 32$, which roughly corresponds to Eddington ratios of $\gtrsim 1$ per cent following the conversion factors from equation (2) of Aird et al. (2018). For the 4XMM sample, we adopt the X-ray fluxes of detected *XMM–Newton* sources from the 4XMM DR11 catalogue (Webb et al. 2020). We convert the X-ray fluxes to L_X assuming a power-law model with Galactic absorption and $\Gamma = 1.7$ following the preference order of 4.5–12 keV band, and 0.2–12 keV band, thus minimizing the effects of X-ray obscuration. About 90 per cent of the X-ray sources in our 4XMM sample have 4.5–12 keV band flux measurements available. For the COSMOS sample, we adopt L_X calculated from Ni et al. (2021b), which is converted from X-ray fluxes following the 2–7 keV, 0.5–7 keV, and

Downloaded from https://academic.oup.com/mnras/article/524/3/4778/7224006 by Rijksuniversiteit Groningen user on 26 September 2023

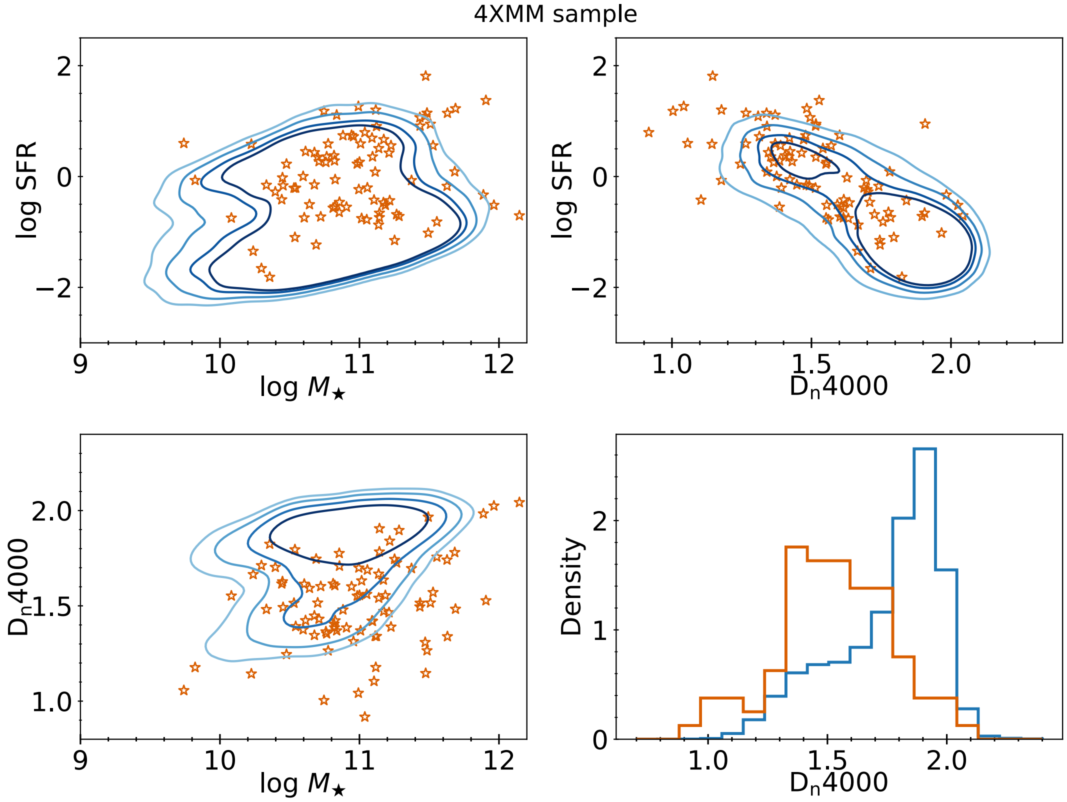

Figure 2. Galaxies in the 4XMM sample in the SFR versus $M_\star$ plane (upper-left), SFR versus D_n4000 plane (upper-right), and D_n4000 versus $M_\star$ plane (bottom-left). The contours encircle 68 per cent, 80 per cent, 90 per cent, and 95 per cent of galaxies. Log $L_X/M_\star > 32$ AGNs are represented by the orange stars. In the bottom-right panel, the D_n4000 distribution of galaxies is represented by the blue histogram; the D_n4000 distribution of log $L_X/M_\star > 32$ AGNs is represented by the orange histogram.

0.5–2 keV order, also assuming the $\Gamma = 1.7$ power-law model. For X-ray sources in the COSMOS sample, ≈ 70 per cent of them have 2–7 keV band flux measurements available, and 0.5–7 keV/0.5–2 keV band flux measurements are used for ≈ 27 per cent/3 per cent of them. In the left panels of Fig. 4, we present the $L_X/M_\star$ distribution of X-ray detected sources which have L_X values greater than the contributions from X-ray binaries (XRBs) in our samples. The XRB luminosity ($L_{X,\,XRB}$) is estimated through a redshift-dependent function of $M_\star$ and SFR (model 269, Fragos et al. 2013), which is derived utilizing observations in Lehmer et al. (2016).

When deriving the AGN fraction, we correct L_X to account for the modest systematic effect from obscuration with correction factors. Utilizing X-ray sources in *Chandra* Deep Field-South (Luo et al. 2017) that have similar X-ray flux level as *Chandra* COSMOS sources but with more counts, Yang et al. (2018) compared the intrinsic L_X from spectral modelling with L_X calculated following the scheme mentioned earlier, and found that the overall underestimation of X-ray emission due to obscuration is ≈ 20 per cent. We apply this correction factor throughout this work for all the L_X values of X-ray detected sources in the COSMOS sample when calculating the AGN fraction. The obscuration correction factor is obtained in a similar manner for the 4XMM sample, utilizing the XMMFITCAT-Z spectral fit catalogue (Ruiz, Georgantopoulos & Corral 2021) that provides intrinsic L_X measurements for 3XMM-DR6 sources. We match X-ray sources in our sample with sources in the XMMFITCAT-Z catalogue that have spec-z available. With this matched sample, we derive the obscuration correction factor needed by obtaining the average value of the intrinsic L_X reported divided by L_X calculated in this work; L_X-dependent weights are applied to the matched sample to recover the L_X distribution of the X-ray AGNs in the whole 4XMM sample. We found that the overall underestimation of X-ray emission due to obscuration is ≈ 10 per cent. We apply this correction factor throughout this work for all the L_X values of X-ray detected sources in the 4XMM sample when calculating the AGN fraction.[4]

When deriving the AGN fraction, we have also taken into account the varying sensitivity of X-ray observations that provide X-ray coverage to our samples. For the 4XMM sample, we derive the sensitivity upper limit of the relevant RapidXMM HealPix from the background level reported at the position of each MPA-JHU galaxy. Following equations (3) and (4) of Chen et al. (2018), we derive the minimum number of counts required for a source to be detected in the 0.2–12 keV band given the background level, and derive the corresponding flux sensitivity with the corresponding energy conversion factor (ECF) which are derived assuming a power-law spectrum with $\Gamma = 1.7$.[5] Since the 4XMM catalogue uses DET_ML = 6 in the 0.2–12 keV band as the source detection criterion, we set the probability of the detected source being a random Poisson fluctuation due to the background as 2.5×10^{-3} when utilizing the

[4]We note that the change in AGN fraction associated with applying the obscuration correction factor is generally much smaller than the statistical uncertainty of AGN fraction. Thus, X-ray absorption should not bias our results materially.

[5]https://www.cosmos.esa.int/web/xmm-newton/epic-upper-limits

Downloaded from https://academic.oup.com/mnras/article/524/3/4778/7224006 by Rijksuniversiteit Groningen user on 26 September 2023

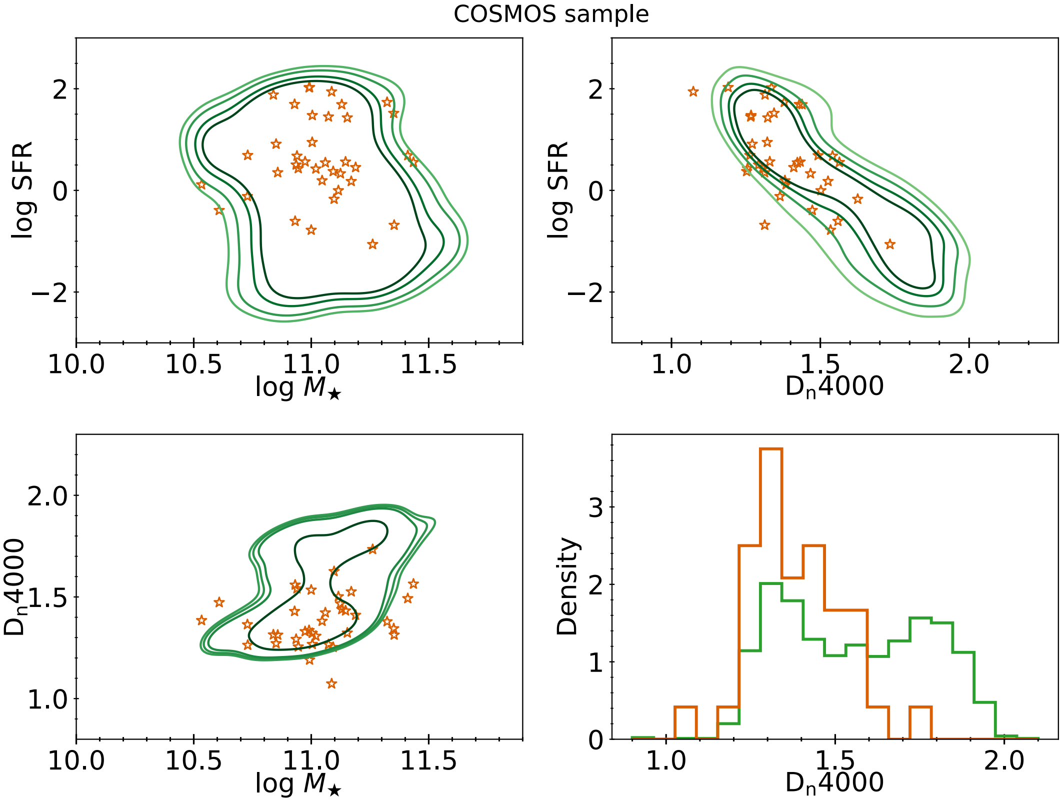

Figure 3. Galaxies in the COSMOS sample in the SFR versus $M_\star$ plane (upper-left), SFR versus D_n4000 plane (upper-right), and D_n4000 versus $M_\star$ plane (bottom-left). The contours encircle 68 per cent, 80 per cent, 90 per cent, and 95 per cent of galaxies. Log $L_X/M_\star > 32$ AGNs are represented by the orange stars. In the bottom-right panel, the D_n4000 distribution of galaxies is represented by the green histogram; the D_n4000 distribution of log $L_X/M_\star > 32$ AGNs is represented by the orange histogram.

equations. For the COSMOS sample, we derive the sensitivity map following the method in Aird, Coil & Georgakakis (2017).

Combining with the redshift information, the lower limit of the L_X of a source in order to be detected, $L_{X,\,limit}$, can be obtained for every galaxy in both the 4XMM sample and the COSMOS sample. We note that a power-law model with Galactic absorption and $\Gamma = 1.7$ is assumed through the whole conversion process. In the right panels of Fig. 4, we present the $L_{X,\,limit}/M_\star$ distribution of galaxies in the 4XMM and COSMOS samples. We only derive AGN fraction utilizing galaxies with log $L_{X,\,limit}/M_\star \leq 32$, that is, these where we have the sensitivities to detect an AGN with log $L_X/M_\star > 32$, if it exists in the given galaxy:

$$f_{\mathrm{AGN,log}\ L_X/M_\star>32} = \frac{N_{\mathrm{det,log}\ L_X/M_\star>32}}{N_{\mathrm{galaxy,log}\ L_{X,limit}/M_\star\leqslant 32}}. \quad (1)$$

The uncertainty of the AGN fraction is obtained via bootstrapping the sample (i.e. randomly drawing the same number of objects from the sample with replacement) 1000 times. For each bootstrapped sample, the AGN fraction is calculated, and the 16th and 84th percentiles of the obtained AGN fraction distribution give the estimation of the 1σ uncertainty. When no AGN is detected in a sample, we report the 1σ confidence upper limits derived following Cameron (2011).

We also estimate the *long-term average BH growth* from $\overline{\mathrm{BHAR}}$ of a given sample of galaxies sharing similar properties, following the method described in Ni et al. (2019, 2021b) that includes contributions from both X-ray detected sources and X-ray undetected sources. We apply the obscuration correction factor mentioned earlier (1.1 for the 4XMM sample and 1.2 for the COSMOS sample) when taking into account the X-ray emission from X-ray detected sources.[6] The X-ray emission of a group of X-ray undetected sources is taken into account via X-ray stacking techniques in the 0.2–12 keV band for the 4XMM sample and the 0.5–7 keV band for the COSMOS sample. With the source counts rate and background counts rate reported in RapidXMM, the net 0.2–12 keV count rate at each galaxy position in the 4XMM sample can be obtained, which is then converted to the 0.2–12 keV flux with the corresponding energy conversion factor derived assuming a power-law spectrum with $\Gamma = 1.7$. For the COSMOS sample, the stacking process is described in Ni et al. (2021b), which gives the 0.5–7 keV net count rate/flux at each galaxy position. We derive the average X-ray luminosity $\overline{L_{X,stack}}$ from the average flux and the average redshift of the stacked sample.

With L_X for individual X-ray detected sources and $\overline{L_{X,stack}}$ for X-ray undetected sources, we can obtain sample-averaged AGN bolometric luminosity following equation (3) of Ni et al. (2021b) assuming the L_X-dependent bolometric correction from Hopkins, Richards & Hernquist (2007):

$$\overline{L_{\mathrm{bol}}} = \frac{\left[\sum_{n=0}^{N_{\mathrm{det}}}(L_X - L_{X,\mathrm{XRB}})k_{\mathrm{bol}}\right] + (\overline{L_{X,\mathrm{stack}}} - \overline{L_{X,\mathrm{XRB}}})N_{\mathrm{non}}\overline{k_{\mathrm{bol}}}}{N_{\mathrm{det}} + N_{\mathrm{non}}} \quad (2)$$

[6] We note that the change in $\overline{\mathrm{BHAR}}$ associated with applying the obscuration correction factor is generally smaller than the statistical uncertainty of $\overline{\mathrm{BHAR}}$. Thus, X-ray absorption should not bias our results materially.

Downloaded from https://academic.oup.com/mnras/article/524/3/4778/7224006 by Rijksuniversiteit Groningen user on 26 September 2023

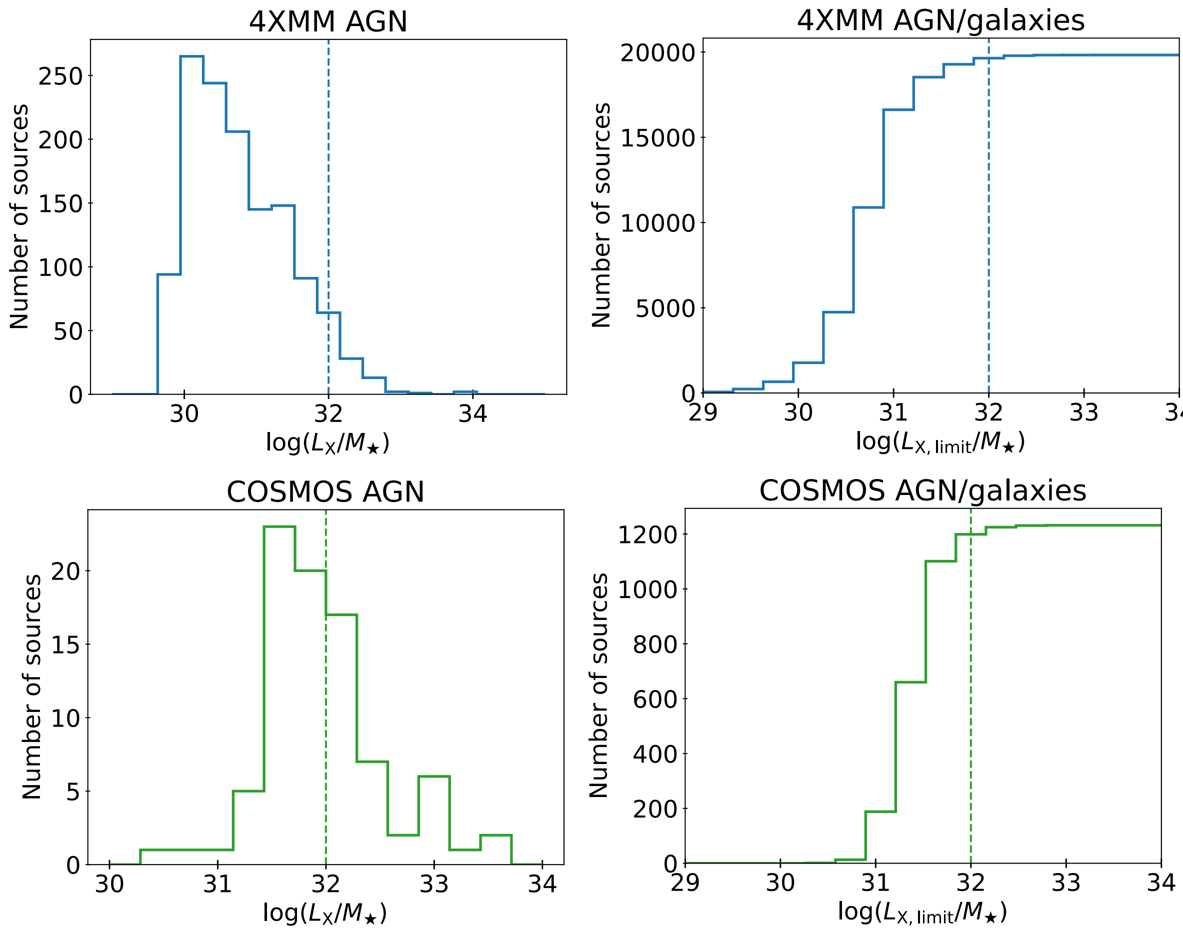

Figure 4. *Left panels:* the observed distribution of log $L_X/M_\star$ for X-ray detected sources in the 4XMM (top left) and COSMOS (bottom left) samples. *Right panels:* the cumulative distribution of the detection limit, log $L_{X,\,limit}/M_\star$ above which an AGN could be detected for all galaxies in the 4XMM (top right) and COSMOS (bottom right) samples. The vertical lines represent the $L_X/M_\star$ limit adopted in our work when calculating AGN fraction. While a significant number of AGNs detected have log $L_X/M_\star$ <32, we note that a large fraction of galaxies in both samples have log $L_{X,\,limit}/M_\star$ ≤32 to enable an unbiased characterization of AGN fraction.

We also subtract the contributions from X-ray binaries (XRBs) from L_X and $\overline{L_{X,stack}}$ before applying the bolometric correction. The contributions from XRBs are generally small compared to the overall X-ray luminosity. Then, sample-averaged AGN bolometric luminosity can be converted to $\overline{\rm BHAR}$ adopting a constant radiative efficiency of 0.1 following equation (4) in Ni et al. (2021b). The uncertainty of $\overline{\rm BHAR}$ is obtained via bootstrapping the sample 1000 times. For each bootstrapped sample, $\overline{\rm BHAR}$ is calculated, and the 16th and 84th percentiles of the obtained $\overline{\rm BHAR}$ distribution give the estimation of the 1σ uncertainty associated with $\overline{\rm BHAR}$ of the sample.

3 ANALYSIS RESULTS

3.1 AGN fraction and $\overline{\rm BHAR}$ as a function of D_n4000

For objects in the 4XMM sample, we bin them into 6 bins with equal number of objects per bin according to their D_n4000 values. Fig. 5(a) shows that the AGN fraction presents a clear decreasing trend with D_n4000 at $D_n4000 \lesssim 1.85$, and slightly increases at $D_n4000 \gtrsim 1.85$. We note that this result will not be materially affected by the $L_X/M_\star$ threshold we adopt (see Appendix B for details). We further plot $\overline{\rm BHAR}$ as a function of D_n4000 for the 4XMM sample (see Fig. 5b). We can see that $\overline{\rm BHAR}$ also decreases as D_n4000 increases from ∼1.25 to ∼1.85. At $D_n4000 \gtrsim 1.85$, the trend appears to reverse, and $\overline{\rm BHAR}$ significantly increases with increasing D_n4000. To account for differences in the average $M_\star$ for galaxies across our D_n4000 bins, we also plot $\overline{{\rm BHAR}/M_\star}$ as a function of D_n4000 (see Fig. 5c), which shows an overall similar trend as $\overline{\rm BHAR}$.

Similarly, we bin objects in the COSMOS sample into 4 bins according to their D_n4000 values, with equal number of objects per bin. For the COSMOS sample, when we calculate AGN fraction as well as $\overline{\rm BHAR}$ for a given subsample in this study, we weight the contribution from each object by the SCOR parameter in the LEGA-C catalogue, which accounts for the selection effects from the parent sample; we also verified that the analysis results do not vary materially when we do not weight each object by SCOR. Fig. 5(d) shows that, at the D_n4000 range we probe ($D_n4000 \approx 1.25$–1.9), AGN fraction decreases with D_n4000 in general. In terms of $\overline{\rm BHAR}$ as well as $\overline{{\rm BHAR}/M_\star}$ (see Figs 5 e and f), similarly, a decreasing trend in general is observed with increasing D_n4000. We note that, at $D_n4000 \lesssim 1.5$, this decreasing trend of AGN fraction, $\overline{\rm BHAR}$, and $\overline{{\rm BHAR}/M_\star}$ is not very significant – the large error bars as a result

Downloaded from https://academic.oup.com/mnras/article/524/3/4778/7224006 by Rijksuniversiteit Groningen user on 26 September 2023

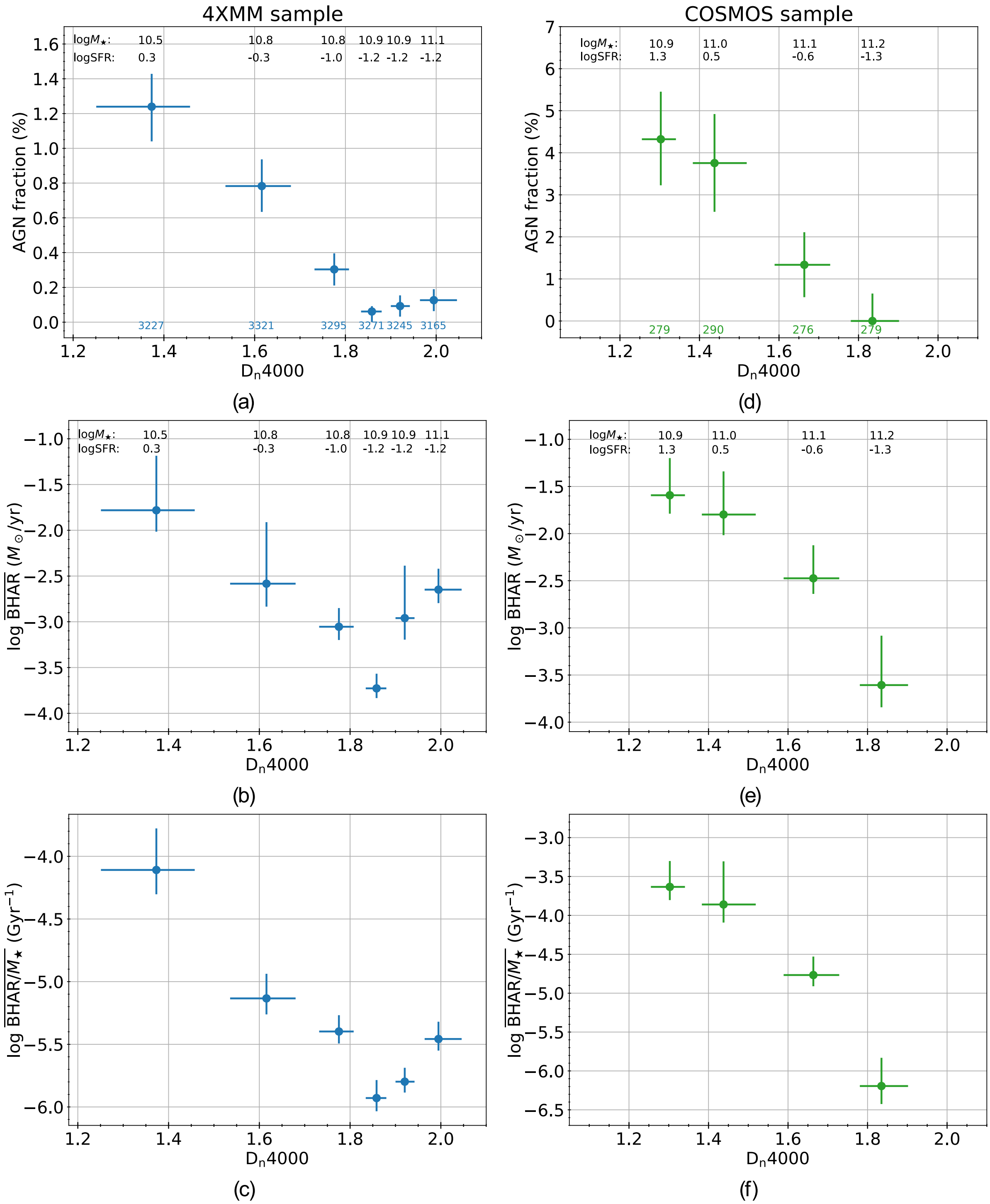

Figure 5. (a) AGN fraction as a function of D_n4000 among galaxies in the 4XMM sample. The horizontal position of each data point represents the median D_n4000 of the sources in each bin, with *x*-axis error bars demonstrating the 16th and 84th percentiles of the D_n4000 values in each bin. The *y*-axis error bars represent the 1σ confidence interval of AGN fraction from bootstrapping. We also list the median log $M_\star$ and log SFR of each bin on the top of the plot. The numbers in the bottom of the plot represent the number of galaxies in each bin used to derive the AGN fraction (with log $L_{\mathrm{X,\,limit}}/M_\star \leq 32$). (b) $\overline{\mathrm{BHAR}}$ as a function of D_n4000 among galaxies in the 4XMM sample. The horizontal position of each data point represents the median D_n4000 of the sources in each bin, with *x*-axis error bars demonstrating the 16th and 84th percentiles of the D_n4000 values in each bin. The *y*-axis error bars represent the 1σ confidence interval of $\overline{\mathrm{BHAR}}$ from bootstrapping. We also list the median log $M_\star$ and log SFR of each bin on the top of the plot. (c) $\overline{\mathrm{BHAR}/M_\star}$ a function of D_n4000 among galaxies in the 4XMM sample. The horizontal position of each data point represents the median D_n4000 of the sources in each bin, with *x*-axis error bars demonstrating the 16th and 84th percentiles of the D_n4000 values in each bin. The *y*-axis error bars represent the 1σ confidence interval of $\overline{\mathrm{BHAR}/M_\star}$ from bootstrapping. (d) Similar to panel (a), but for AGN fraction as a function of D_n4000 among galaxies in the COSMOS sample. (e) Similar to panel (b), but for $\overline{\mathrm{BHAR}}$ as a function of D_n4000 among galaxies in the COSMOS sample. (f) Similar to panel (c), but for $\overline{\mathrm{BHAR}/M_\star}$ as a function of D_n4000 among galaxies in the COSMOS sample.

Downloaded from https://academic.oup.com/mnras/article/524/3/4778/7224006 by Rijksuniversiteit Groningen user on 26 September 2023

of the limited sample size prohibits us from drawing any significant conclusion.

We further investigate AGN fraction and $\overline{\rm BHAR}$ in different $M_\star$ ranges for both the 4XMM sample and the COSMOS sample; the results can be seen in Fig. 6. We can see that for different $M_\star$ ranges in the 4XMM sample, AGN fraction, $\overline{\rm BHAR}$, and $\overline{{\rm BHAR}/M_\star}$ also decrease with $\rm D_n4000$ at $\rm D_n4000 \lesssim 1.9$. The increasing trend of $\overline{\rm BHAR}$ at larger $\rm D_n4000$ is more prominent among objects with $11 < \log M_\star \le 12$. For different $M_\star$ ranges in the COSMOS sample, we also observe decreasing trends of AGN fraction, $\overline{\rm BHAR}$, and $\overline{{\rm BHAR}/M_\star}$ with $\rm D_n4000$, though we note that for $\rm D_n4000 \lesssim 1.5$ objects with $10 < \log M_\star \le 11$, the decreasing trend is not very significant, which might be caused by the limited sample size.

3.2 AGN fraction and $\overline{\rm BHAR}$ as a function of $\rm D_n4000$ when controlling for other host-galaxy parameters

We note that, while in Section 3.1 we characterized the incidence of X-ray AGNs among galaxies with different stellar ages (as $\rm D_n4000$ is closely associated with the age of the stellar populations), we can still not quantify how the difference in $\rm D_n4000$ (which indicates the difference in the mean stellar population age) directly affects AGN activity and BH growth, as host-galaxy properties such as $M_\star$ and SFR vary across different $\rm D_n4000$ bins, which are known to closely related with AGN activity and BH growth.

We thus would like to study AGN fraction and $\overline{\rm BHAR}$ as a function of $\rm D_n4000$ when controlling for other host-galaxy parameters. To achieve this, for each bin (except the first and last bins) of galaxies in the 4XMM sample in Fig. 5, we sort this subsample with their $\rm D_n4000$ values, and keep the central 1/3 of the objects to form a reference bin.[7] The first 1/3 of the objects are merged with the bin on the left, and the last 1/3 of the objects are merged with the bin on the right. We then select the nearest neighbour of objects in the reference bin among objects in its left/right bin in the $M_\star$, SFR, and z space utilizing the `NearestNeighbors` algorithm in the `scikit-learn` python package, to constitute two comparison samples with similar $M_\star$, SFR, and z properties, but one with smaller $\rm D_n4000$ and one with larger $\rm D_n4000$. In Fig. 7, we show AGN fractions of all these subsamples, with each set of subsamples sharing similar $M_\star$, SFR, and z values represented by different colours and symbols. Comparing within each subsample set reveals how AGN fraction varies with $\rm D_n4000$ when controlling for other host-galaxy parameters, and a significant decreasing trend is observed within each subsample set at $\rm D_n4000 \lesssim 1.9$.[8] We also demonstrate that our results hold when defining the AGN fraction by an $L_{\rm X}$ limit of 10^{42} erg s^{-1} in the Appendix C. We show $\overline{\rm BHAR}$ and $\overline{{\rm BHAR}/M_\star}$ of all these subsamples as well in Fig. 7, with each set of subsamples sharing similar $M_\star$, SFR, and z values represented by different colours and symbols. Comparing within each subsample set shows that $\overline{\rm BHAR}$ and $\overline{{\rm BHAR}/M_\star}$ also decrease with $\rm D_n4000$ at $\rm D_n4000 \lesssim 1.9$ when controlling for $M_\star$, SFR, and z.[9] At $\rm D_n4000 \gtrsim 1.9$, $\overline{\rm BHAR}$ and $\overline{{\rm BHAR}/M_\star}$ increase with $\rm D_n4000$ when controlling for $M_\star$, SFR, and z.

Similarly, we study how AGN fraction and BH growth vary with $\rm D_n4000$ within subsample sets when controlling for other host-galaxy parameters for the COSMOS sample. The results are shown in Fig. 8. We also observe a trend of decreasing AGN fraction, $\overline{\rm BHAR}$ and $\overline{{\rm BHAR}/M_\star}$ with $\rm D_n4000$, similar to that seen at lower redshifts in our 4XMM sample, although at $\rm D_n4000 \lesssim 1.5$ this trend has a relatively low significance level.

We also show that host morphological properties do not affect the results in this subsection materially in Appendix D.

3.3 The incidence of low-accretion-rate AGN as a function of $\rm D_n4000$ compared with $\log L_{\rm X}/M_\star > 32$ AGN

In Section 3.1, we find that for objects in the 4XMM sample, while $\overline{\rm BHAR}$ and $\overline{{\rm BHAR}/M_\star}$ significantly increase with $\rm D_n4000$ at $\rm D_n4000 \gtrsim 1.85$, the AGN fraction does not increase significantly, which might be caused by our definition for AGNs, as we only look at $\log L_{\rm X}/M_\star > 32$ AGNs in Section 3.1 and do not take low-accretion-rate AGNs into account when calculating the AGN fraction. This inspired us to examine the incidence of low-accretion-rate AGN as a function of $\rm D_n4000$. As stated in Section 2.4, we only consider an X-ray detected source as AGN when $L_{\rm X}$ is greater than the contribution from XRBs. As can be seen in Fig. 4, we have a considerable number of AGNs with $\log L_{\rm X}/M_\star \le 32$ detected in the 4XMM sample, and there are also a large number of galaxies in the 4XMM sample with $\log L_{\rm X,\,limit}/M_\star \le 32$. We thus use these objects to study how the fraction of AGNs with $31 < \log L_{\rm X}/M_\star < 32$ varies as a function of $\rm D_n4000$, and the result is shown in Fig. 9. We can see that the fraction increases at $\rm D_n4000 \gtrsim 1.85$ obviously.

We further probe if this increase of low-accretion-rate AGN fraction with $\rm D_n4000$ is linked with $M_\star$, by studying the low-accretion-rate AGN fraction as a function of $\rm D_n4000$ in different $M_\star$ bins. As we can see in Fig. 10, for galaxies/AGN with $\log M_\star < 11.5$, AGNs tend to live among younger galaxies. In contrast, for galaxies/AGNs with $\log M_\star > 11.5$, the fraction of AGNs with $31 < \log L_{\rm X}/M_\star < 32$ increases with $\rm D_n4000$. When we perform the same analyses for $\log L_{\rm X}/M_\star > 32$ AGNs, we found that the fractions of $\log L_{\rm X}/M_\star > 32$ AGNs at different $M_\star$ ranges all drop with $\rm D_n4000$.

3.4 Comparing with the incidence of AGNs selected at different wavelength bands

We note that our results in previous subsections are based on X-ray-selected AGNs. While X-ray selection is known to be able to provide the most complete and unbiased sample of AGNs, we would like to test how different AGN selection methods could potentially affect our results. In this subsection, we select AGNs based purely on detection in a waveband in a given catalogue, in contrast to the careful measurement of AGN fraction to specific BH accretion rate limits (corrected for any incompleteness) adopted in our X-ray-based analyses earlier. Extending this more robust approach to MIR- and radio-selected samples is deferred to a future work.

[7]While choosing this relatively small subsample size reduces the statistical power compared to the larger bin size used in Section 3.1, these narrower bins are necessary to ensure sufficient sources with similar $M_\star$, SFR, and z values in the adjacent bins that are used to create the comparison samples.

[8]We note that while AGN fraction varies with $\rm D_n4000$, it also varies when other host-galaxy properties change, so that at a fixed $\rm D_n4000$, the AGN fraction from different subsamples differs due to the differences in $M_\star$ and SFR.

[9]While X-ray emission from normal star-forming galaxies has potential dependence on stellar ages (e.g. Gilbertson et al. 2022), the XRB contribution is little among the objects we investigated (∼ 5–15 per cent), so should not bias our results.

Downloaded from https://academic.oup.com/mnras/article/524/3/4778/7224006 by Rijksuniversiteit Groningen user on 26 September 2023

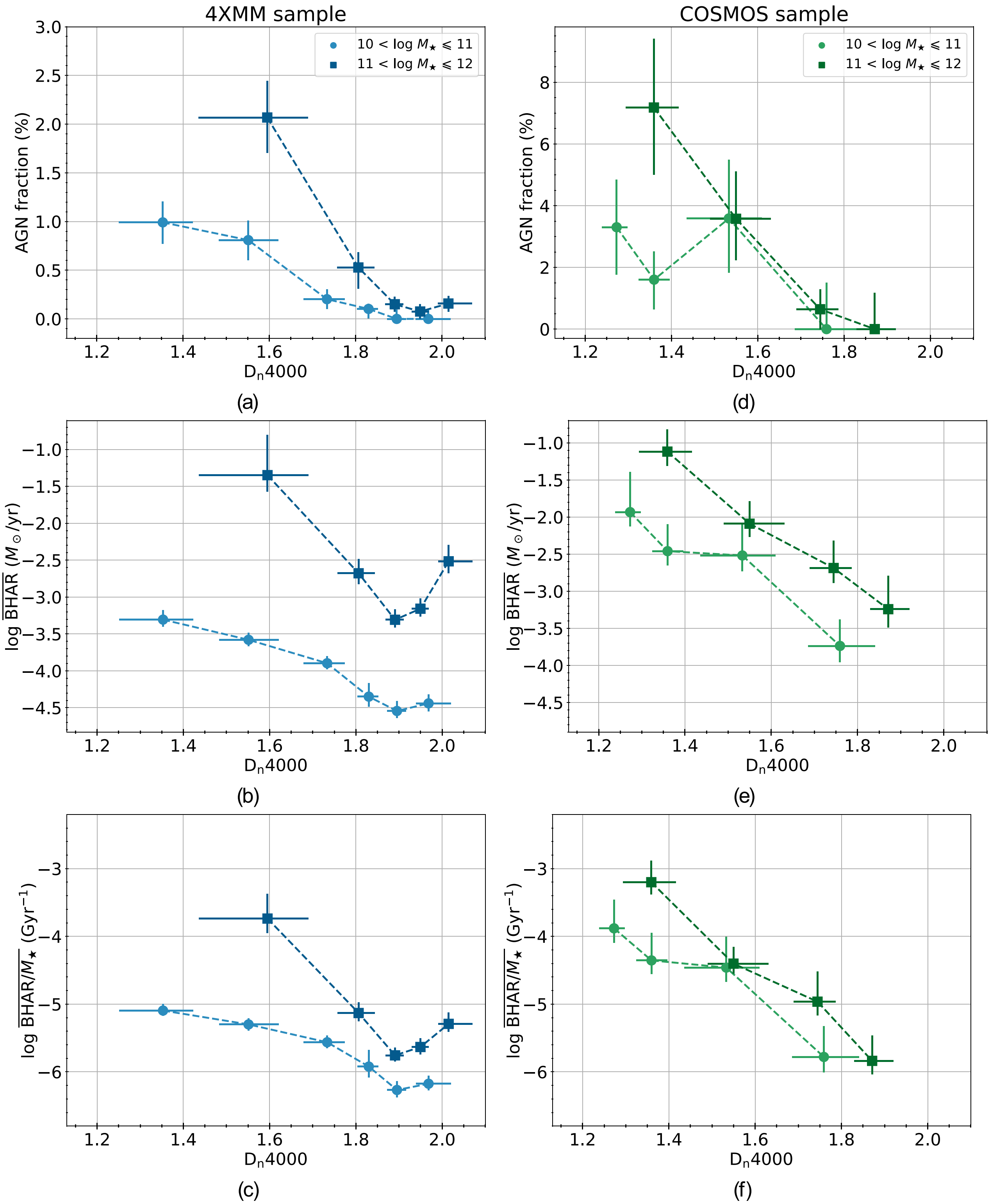

Figure 6. (a) AGN fraction as a function of $\mathrm{D_n}4000$ among galaxies in two $M_\star$ bins (represented by different colours and symbols) in the 4XMM sample. The horizontal position of each data point represents the median $\mathrm{D_n}4000$ of the sources in each bin, with *x*-axis error bars demonstrating the 16th and 84th percentiles of the $\mathrm{D_n}4000$ values in each bin. The *y*-axis error bars represent the 1σ confidence interval of AGN fraction from bootstrapping. (b) $\overline{\mathrm{BHAR}}$ as a function of $\mathrm{D_n}4000$ among galaxies in the 4XMM sample. The horizontal position of each data point represents the median $\mathrm{D_n}4000$ of the sources in each bin, with *x*-axis error bars demonstrating the 16th and 84th percentiles of the $\mathrm{D_n}4000$ values in each bin. The *y*-axis error bars represent the 1σ confidence interval of $\overline{\mathrm{BHAR}}$ from bootstrapping. (c) $\overline{\mathrm{BHAR}/M_\star}$ as a function of $\mathrm{D_n}4000$ among galaxies in the 4XMM sample. The horizontal position of each data point represents the median $\mathrm{D_n}4000$ of the sources in each bin, with *x*-axis error bars demonstrating the 16th and 84th percentiles of the $\mathrm{D_n}4000$ values in each bin. The *y*-axis error bars represent the 1σ confidence interval of $\overline{\mathrm{BHAR}/M_\star}$ from bootstrapping. (d) Similar to panel (a), but for AGN fraction as a function of $\mathrm{D_n}4000$ among galaxies in two $M_\star$ bins in the COSMOS sample. (e) Similar to panel (b), but for $\overline{\mathrm{BHAR}}$ as a function of $\mathrm{D_n}4000$ among galaxies in two $M_\star$ bins in the COSMOS sample. (f) Similar to panel (c), but for $\overline{\mathrm{BHAR}/M_\star}$ as a function of $\mathrm{D_n}4000$ among galaxies in two $M_\star$ bins in the COSMOS sample.

Downloaded from https://academic.oup.com/mnras/article/524/3/4778/7224006 by Rijksuniversiteit Groningen user on 26 September 2023

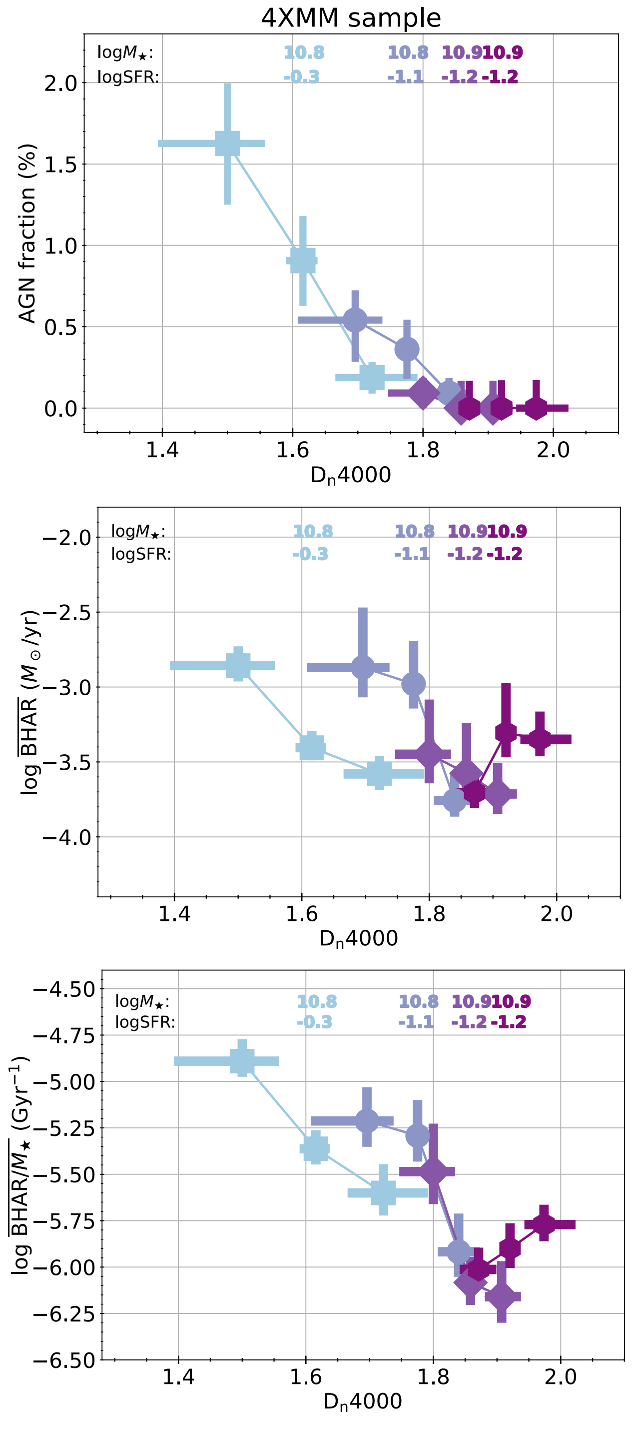

Figure 7. *Top*: AGN fraction as a function of D_n4000 among galaxies in the 4XMM sample when controlling for $M_\star$, SFR, and z. Different symbols and colours represent a set of subsamples with similar $M_\star$, SFR, and z values (as listed on top of the panel with the same colour). The horizontal position of each data point represents the median D_n4000 of the sources in each sample, with x-axis error bars demonstrating the 16th and 84th percentiles of the D_n4000 values. The y-axis error bars represent the 1σ confidence interval of AGN fraction from bootstrapping. *Middle:* similar to the top panel, but for $\overline{\mathrm{BHAR}}$ as a function of D_n4000 among galaxies in the 4XMM sample when controlling for $M_\star$, SFR, and z. *Bottom:* similar to the top panel, but for $\overline{\mathrm{BHAR}/M_\star}$ as a function of D_n4000 among galaxies in the 4XMM sample when controlling for $M_\star$, SFR, and z.

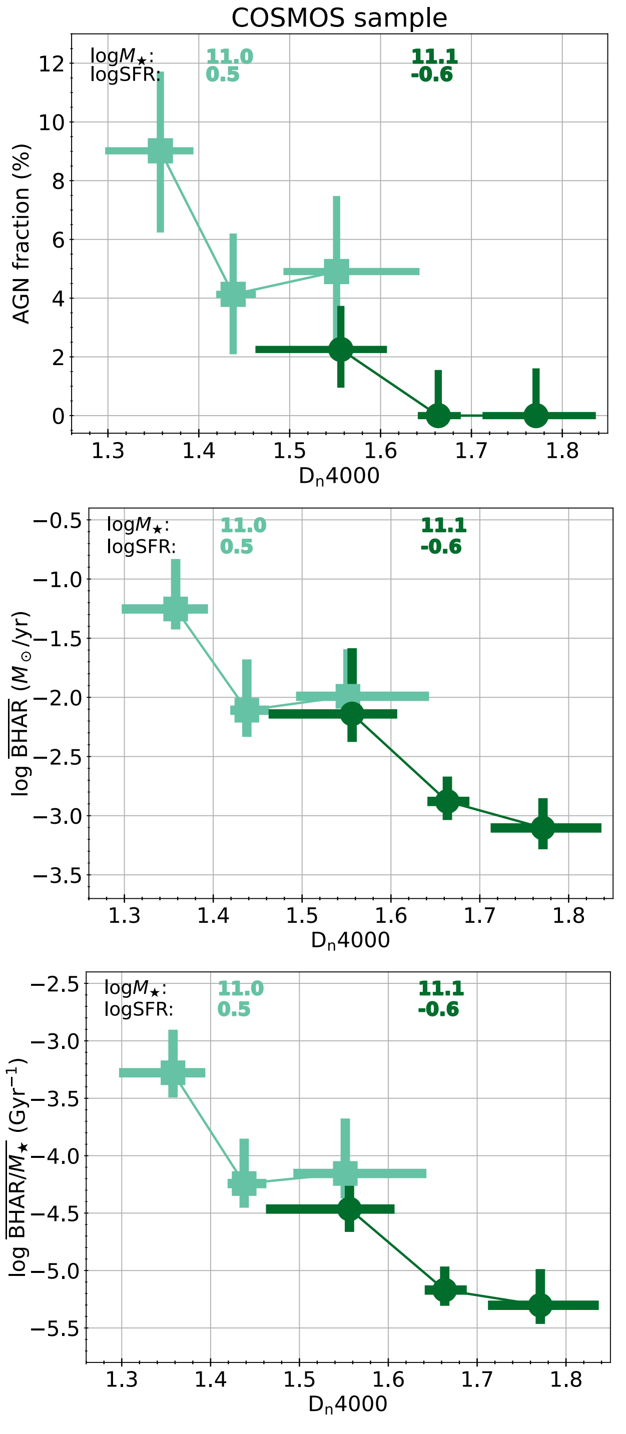

Figure 8. *Top*: similar to the top panel of Fig. 7, but for AGN fraction as a function of D_n4000 when controlling for $M_\star$, SFR, and z among galaxies in the COSMOS sample. *Middle:* similar to the middle panel of Fig. 7, but for $\overline{\mathrm{BHAR}}$ as a function of D_n4000 when controlling for $M_\star$, SFR, and z among galaxies in the COSMOS sample. *Bottom:* similar to the middle panel of Fig. 7, but for $\overline{\mathrm{BHAR}/M_\star}$ as a function of D_n4000 when controlling for $M_\star$, SFR, and z among galaxies in the COSMOS sample.

Downloaded from https://academic.oup.com/mnras/article/524/3/4778/7224006 by Rijksuniversiteit Groningen user on 26 September 2023

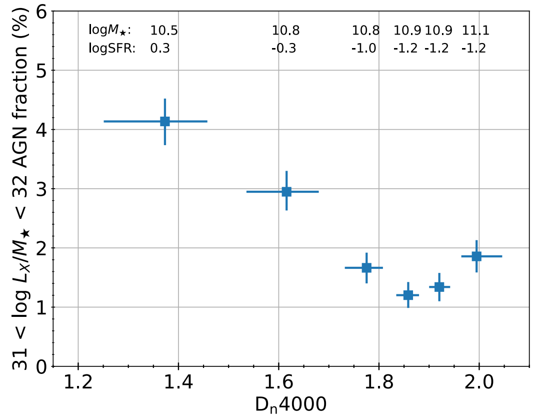

Figure 9. 31 < log $L_X/M_\star$ < 32 AGN fraction as a function of D_n4000 among galaxies in the 4XMM sample. The horizontal position of each data point represents the median D_n4000 of the sources in each bin, with *x*-axis error bars demonstrating the 16th and 84th percentiles of the D_n4000 values in each bin. The *y*-axis error bars represent the 1σ confidence interval of AGN fraction from bootstrapping. We also list the median log $M_\star$ and log SFR value of each bin on the top of the plot.

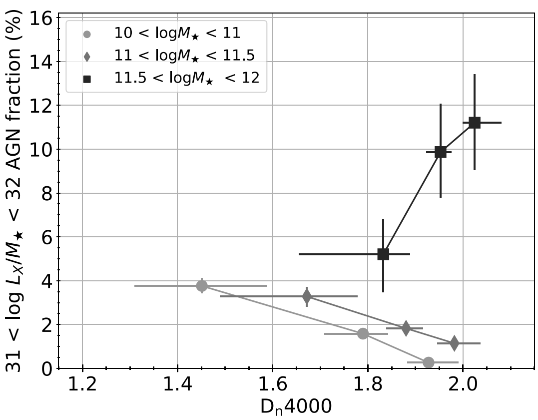

Figure 10. 31 < log $L_X/M_\star$ < 32 AGN fraction as a function of D_n4000 among galaxies with different $M_\star$ ranges in the 4XMM sample; different symbols and colours represent subsamples of galaxies with different $M_\star$ ranges. The horizontal position of each data point represents the median D_n4000 of the sources in each bin, with *x*-axis error bars demonstrating the 16th and 84th percentiles of the D_n4000 values in each bin. The *y*-axis error bars represent the 1σ confidence interval of AGN fraction from bootstrapping.

3.4.1 *Comparing with the incidence of AGNs selected at MIR*

We obtain a MIR-selected AGN sample among MPA-JHU galaxies in the main SDSS galaxy sample from the R90 catalogue of Assef et al. (2018), which consists of AGN candidates with 90 per cent reliability. We perform the same analyses as those in Section 3.2 to check how the fraction of MIR-selected AGNs varies with D_n4000 when controlling for host-galaxy properties, and whether the observed trend is consistent with what we observed in the X-ray. The analysis results are shown in Fig. 11. We observe a similar trend as these in Section 3.2: when controlling for host-galaxy properties, the fraction of MIR-selected AGNs decreases with D_n4000 at D_n4000 $\lesssim$ 1.9. As MIR-selected AGNs are generally biased against AGNs in most massive galaxies, the MIR-selected AGN fraction at high D_n4000 in Fig. 11 is too small to observe any trend.

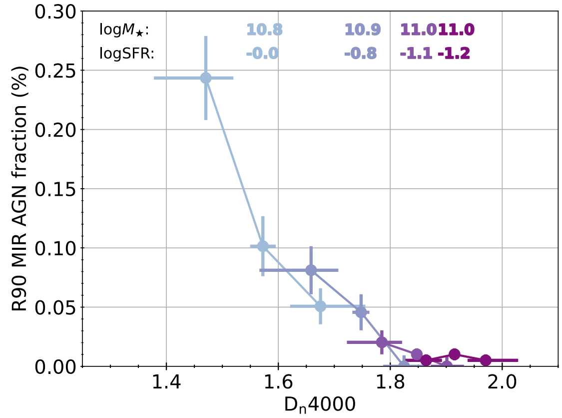

Figure 11. MIR AGN fraction as a function of D_n4000 among SDSS galaxies when controlling for $M_\star$, SFR, and *z*. Different colours represent a set of subsamples with similar $M_\star$, SFR, and *z* values (as listed on top of the panel with the same colour). The horizontal position of each data point represents the median D_n4000 of the sources in each sample, with *x*-axis error bars demonstrating the 16th and 84th percentiles of the D_n4000 values. The *y*-axis error bars represent the 1σ confidence interval of AGN fraction from bootstrapping.

3.4.2 *Comparing with the incidence of AGNs selected at radio wavelength*

To study how the fraction of radio-selected AGNs varies with D_n4000, we utilize the radio AGN sample from Best & Heckman (2012), constructed by combining SDSS data with the NRAO (National Radio Astronomy Observatory) VLA (Very Large Array) Sky Survey (NVSS) and the Faint Images of the Radio Sky at Twenty centimetres (FIRST) survey. The classification of radio AGNs into high-excitation radio galaxies (HERGs) and low-excitation radio galaxies (LERGs) is available for this sample. This radio AGN sample mainly consists of LERGs (that have small Eddington ratios; < 1 per cent), with a small fraction of HERGs reported. We match these radio AGNs to MPA-JHU galaxies in the main SDSS galaxy sample, and perform the same analyses as those in Section 3.2 to check how the fraction of radio-selected AGNs in general, HERGs and LERGs, vary with D_n4000 when controlling for host-galaxy properties. The analysis results are shown in Fig. 12.

Unlike X-ray-selected AGNs and MIR-selected AGNs, radio-selected AGNs in this sample (dominated by the LERG population) are more likely to be found among old galaxies with large D_n4000 values. This has been known for decades, as the radio AGN fraction is strongly linked with $M_\star$ (e.g. Best et al. 2005). As can be seen in the right panel of Fig. 12, HERG fraction always decreases with D_n4000 when controlling for host-galaxy properties at D_n4000 $\lesssim$ 1.9, similar to what we found for the X-ray-selected AGN fraction. In the middle panel of Fig. 12, we can see that at D_n4000 $\lesssim$ 1.7, the LERG fraction also decreases with D_n4000 when controlling for $M_\star$, SFR, and *z*. In contrast, at high D_n4000 values (D_n4000 $\gtrsim$ 1.7), the LERG fraction increases with D_n4000 when controlling for other parameters, similar to what we found among low-accretion-rate X-ray-selected AGNs among massive (log $M_\star$ $\gtrsim$ 11.5) galaxies.

4 DISCUSSIONS

In Section 3.1, we characterize how the log $L_X/M_\star$ > 32 AGN fraction, $\overline{\mathrm{BHAR}}$, and $\overline{\mathrm{BHAR}/M_\star}$ vary with D_n4000 at two different redshift ranges; in Section 3.2, we found that when controlling for

Downloaded from https://academic.oup.com/mnras/article/524/3/4778/7224006 by Rijksuniversiteit Groningen user on 26 September 2023

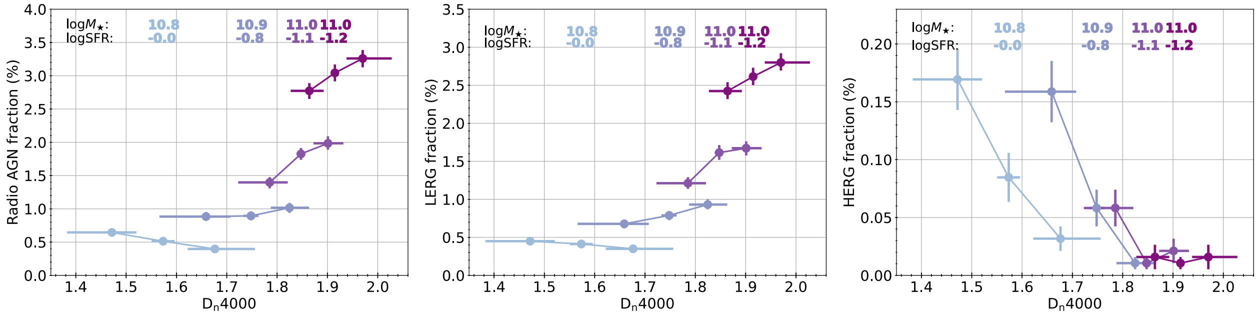

Figure 12. *Left panel:* radio AGN fraction as a function of D_n4000 among SDSS galaxies when controlling for $M_\star$, SFR, and z. Different colours represent a set of subsamples with similar $M_\star$, SFR, and z values (as listed on top of the panel with the same colour). The horizontal position of each data point represents the median D_n4000 of the sources in each sample, with x-axis error bars demonstrating the 16th and 84th percentiles of the D_n4000 values. The y-axis error bars represent the 1σ confidence interval of AGN fraction from bootstrapping. *Middle panel:* similar to the left panel, but for LERGs. *Right panel:* similar to the left panel, but for HERGs.

host-galaxy properties ($M_\star$, SFR, and z), the fraction of $\log L_X/M_\star > 32$ AGNs and $\overline{\mathrm{BHAR}}$ decrease with D_n4000 among galaxies with $D_n4000 \lesssim 1.9$. We discuss the potential reason for these findings in Section 4.1. In Section 3.3, we found that among the most massive galaxies at low redshift, the fraction of $31 < \log L_X/M_\star < 32$ AGNs increases with D_n4000, and we discuss the potential reason for this as well as the increase of $\overline{\mathrm{BHAR}/M_\star}$ among the oldest galaxies at low redshift in Section 4.2.

4.1 Stellar mass loss as a potential fuel for BH growth

We showed in Section 3.1 that galaxies in both the 4XMM sample and COSMOS sample display a decrease of AGN fraction, $\overline{\mathrm{BHAR}}$, or $\overline{\mathrm{BHAR}/M_\star}$ with D_n4000 at $D_n4000 \lesssim 1.9$, suggesting a higher level of AGN activity and BH growth among younger galaxies. It is plausible that among younger galaxies, higher amounts of fuels are available for the central BHs. Kauffmann & Heckman (2009) argue that stellar mass loss may serve as an important source of fuel for BHs when the cold gas supply is not plentiful. As younger galaxies have higher stellar mass loss rates, a higher level of AGN activity and BH growth among younger galaxies is expected if recycled gas from stellar mass loss serves as an important fuelling source, consistent with our finding. We further plot $\overline{\mathrm{BHAR}/M_\star}$ among star-forming galaxies and quiescent galaxies in both the 4XMM sample and the COSMOS sample as a function of D_n4000 separately in Fig. 13, and compare with stellar mass loss rate expected at a given D_n4000.[10] We use PYTHON-FSPS (Conroy, Gunn & White 2009; Conroy & Gunn 2010) to predict how stellar mass loss rates vary as a function of D_n4000. We adopt the universal initial mass function as parametrized by Chabrier (2003). Star-forming histories are generated using a range of formation times, with exponential decline time-scales or delayed-exponential time-scales ranging from 0.1 Gyr to 3 Gyr. In the background of Fig. 13, we show the predicted stellar mass loss rate (in units of the fraction of the stellar mass returned per Gyr) scaled by a factor of 1/5000 as a function of D_n4000 for galaxies with different star-forming histories. We could see that $\overline{\mathrm{BHAR}}$ per solar mass roughly traces the stellar mass loss per solar mass predicted by the FSPS model divided by a factor of $\sim$5000 among almost all galaxies in the 4XMM sample (except for the $D_n4000 \approx 2$ bin), indicating that stellar mass loss might be the fuelling source for these galaxies: not only for the quiescent galaxies, but also for the star-forming galaxies. For the whole 4XMM sample, the $\log \overline{\mathrm{BHAR}}/\overline{\mathrm{SFR}}$ value is ≈ -2.5, and the scaling factor of 5000 is consistent with this value assuming that stellar mass loss also serves as the major fuel for star formation and the fraction of gas that turns into stars is $\sim 0.03 - 0.4$ (e.g. Ciotti & Ostriker 2007). As the galaxies in our 4XMM sample and COSMOS sample have similar median/mean $M_\star$ and velocity dispersion, we assume that the fraction of stellar mass loss that can be captured by the central BH is similar for these two samples. If we compare the $\overline{\mathrm{BHAR}}$ per solar mass in the COSMOS sample with the stellar mass loss rate scaled by a factor of 1/5000, we could see that $\overline{\mathrm{BHAR}/M_\star}$ only traces stellar mass loss rate well among the oldest galaxies in the COSMOS sample. Among most galaxies in the COSMOS sample, it is likely that the cold gas in the galaxy with origins other than the stellar mass loss is capable of serving as the major fuel for both the BH and the star formation process.

The decreasing trend of X-ray AGN fraction and $\overline{\mathrm{BHAR}}$ with D_n4000 when controlling for other host-galaxy properties among most galaxies in the 4XMM sample and COSMOS sample observed in Section 3.2 further supports this scenario. A similar trend is also observed in the case of MIR-selected AGN fraction and HERG fraction at low redshift (see Figs 11 and 12). As stellar population synthesis models predict that stellar mass loss rates decline as a function of mean stellar age (e.g. see the background dots in Fig. 13), we could see that the difference in X-ray AGN fraction (or $\overline{\mathrm{BHAR}}$) when controlling for $M_\star$, SFR, and z is smaller at larger D_n4000. From the bottom panel of Fig. 7 (4XMM sample), we observe a $\sim 1 \times 10^{-5}/5 \times 10^{-6}/2 \times 10^{-6}\,\mathrm{Gyr}^{-1}$ drop in $\overline{\mathrm{BHAR}/M_\star}$ associated with a $\sim 3 \times 10^{-2}/8 \times 10^{-3}/4 \times 10^{-3}\,\mathrm{Gyr}^{-1}$ drop in stellar mass loss rate (inferred from the difference in D_n4000) in the first/second/third D_n4000 subsample set. In the fourth D_n4000 subsample set, we observe an increase in $\overline{\mathrm{BHAR}}$ when D_n4000 increases. From the bottom panel of Fig. 8 (COSMOS sample), we observe a $\sim 5 \times 10^{-4}/3 \times 10^{-5}\,\mathrm{Gyr}^{-1}$ drop in $\overline{\mathrm{BHAR}/M_\star}$ associated with a $\sim 9 \times 10^{-2}/2 \times 10^{-2}\,\mathrm{Gyr}^{-1}$ drop in stellar mass loss rate in the first/second D_n4000 subsample set. Generally, higher levels of BH growth are associated with more stellar mass loss. At the same time, the relation between the difference in $\overline{\mathrm{BHAR}/M_\star}$ associated with the difference in stellar mass loss rate is not exactly linear, that is, the predicted change in the stellar mass loss rate based on the change in D_n4000 does not result in a consistent change in $\overline{\mathrm{BHAR}/M_\star}$ across all the subsamples used in Figs 7 and 8. While

[10]The separation between star-forming galaxies and quiescent galaxies is performed following the criterion in Section 2.4 of Ni et al. (2021b), which utilizes the star formation main sequence.

Downloaded from https://academic.oup.com/mnras/article/524/3/4778/7224006 by Rijksuniversiteit Groningen user on 26 September 2023

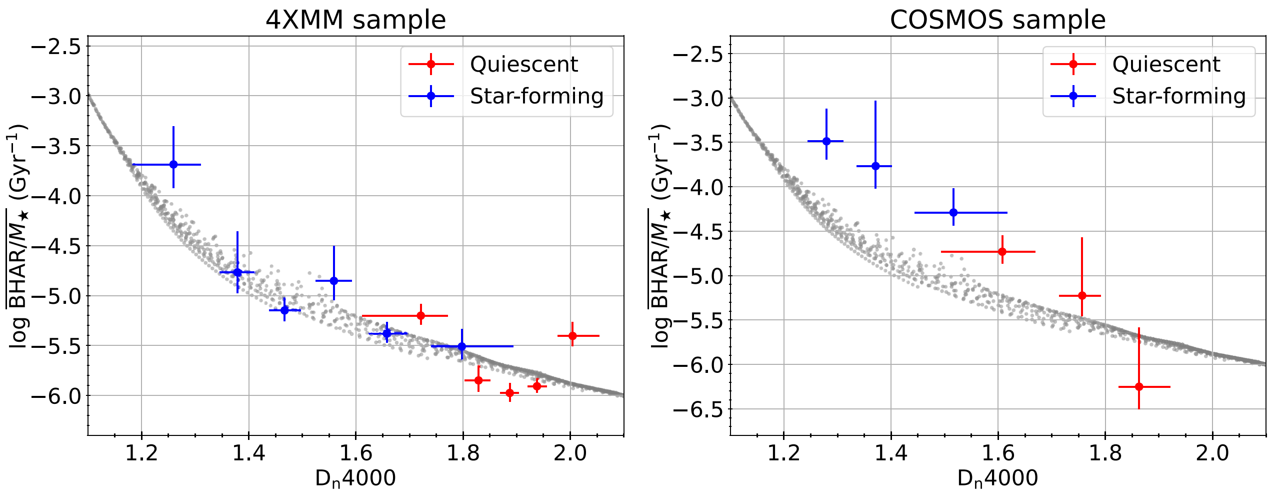

Figure 13. *Left panel:* $\overline{\mathrm{BHAR}/M_\star}$ as a function of $\mathrm{D_n}4000$ among star-forming/quiescent galaxies in the 4XMM sample, represented by the blue/red symbols. The horizontal position of each data point represents the median $\mathrm{D_n}4000$ of the sources in each bin, with *x*-axis error bars demonstrating the 16th and 84th percentiles of the $\mathrm{D_n}4000$ values in each bin. The *y*-axis error bars represent the 1σ confidence interval of $\overline{\mathrm{BHAR}/M_\star}$ from bootstrapping. In the background, stellar mass loss rate per stellar mass unit per Gyr scaled by a factor of 1/5000 is shown as grey dots. *Right panel:* similar to the left panel, but for $\overline{\mathrm{BHAR}/M_\star}$ as a function of $\mathrm{D_n}4000$ among star-forming/quiescent galaxies in the COSMOS sample.

stellar mass loss could be one potential fuelling mechanism, it is not always the dominant fuelling mechanism. Also, the fraction of stellar mass loss that could be accreted by the central BH is likely to vary among galaxies, depending on other galaxy properties such as their total stellar masses (which is clearly indicated in Fig. 6: more massive galaxies tend to accrete stellar mass loss more efficiently, which is expected as they have larger potential wells and larger BH masses), morphologies, and star formation histories.

In Fig. 14, we plot the stellar mass loss per stellar mass unit per Gyr as a function of $\mathrm{D_n}4000$, as well as scaled $\overline{\mathrm{BHAR}/M_\star}$ of galaxies in subsamples with different $M_\star$ ranges (the scaling factor is chosen so that the lowest $\overline{\mathrm{BHAR}/M_\star}$ align with stellar mass loss rate) for both the 4XMM sample and COSMOS sample.[11] For the 4XMM sample, $\overline{\mathrm{BHAR}/M_\star}$ does not track stellar mass loss well among log $M_\star > 11$ galaxies. This might be due to the fact that the accretion efficiency from recycled gas is closely related to other factors in addition to $M_\star$, or there are other gas sources for the most massive galaxies at low redshift. It is also plausible that the onset of the cooling of recycled gas takes several Gyrs to happen among these most massive galaxies due to, e.g. AGN feedback (more massive galaxies tend to host more luminous AGNs that drive stronger outflows and exhibit more powerful jets), so that $\overline{\mathrm{BHAR}/M_\star}$ does not track instantaneous stellar mass loss rate at the scale of $\lesssim 100$ Myrs, but stellar mass loss accumulated in the past several Gyrs. In the background of Fig. 14, we also plot the average stellar mass loss rate of stellar populations with different star formation histories over the past 1, 2, and 3 Gyr, represented by the yellow, orange, and red dots. We can see that if the cooling and accretion of the accumulated hot recycled gas is not a process that happens in a less than 1 Gyr time-scale, it could explain the high $\overline{\mathrm{BHAR}/M_\star}$ among the relatively young massive galaxies in the 4XMM sample. If this is the case, it is also plausible that recycled gas contributes significantly to the fuel of BHs among star-forming galaxies in the COSMOS sample (see the right panel of Fig. 14).

We note that it is also plausible that metallicity plays a role here, as the higher the $\mathrm{D_n}4000$, the higher the metallicity (e.g. Gallazzi et al. 2005), and it has been argued that BH growth might be more efficient in the low-metallicity regime (e.g. Toyouchi et al. 2019). Disentangling the effects of age and metallicity would need a large and complete high-signal-to-noise spectroscopic sample from future surveys (e.g. DESI Collaboration et al. 2016; de Jong et al. 2019). Since $\mathrm{D_n}4000$ is primarily utilized as an age-sensitive parameter (e.g. Kauffmann et al. 2003; Gallazzi et al. 2005; Kauffmann & Heckman 2009; Wu et al. 2018) and we do not observe similarly significant trends when utilizing more metallicity-sensitive parameters (e.g. [MgFe]′, [$\mathrm{Mg_2Fe}$]; see Gallazzi et al. 2005 and references therein), we interpret the link between AGN activity/BH growth with $\mathrm{D_n}4000$ mainly a result of the variation of AGN activity/BH growth among galaxies with different stellar population ages.

We also caution that we do not observe a solid decreasing AGN fraction or $\overline{\mathrm{BHAR}}$ trend with $\mathrm{D_n}4000$ at $\mathrm{D_n}4000 \lesssim 1.5$ for the COSMOS sample. The lack of a clear trend might be due to the limited sample size; it might be due to gas with origins other than stellar mass loss serving as the dominating fuel which 'washes out' the role of stellar mass loss; it might also be attributed to a scenario where the recycled gas from stellar mass loss can not easily cool down or reach the BH in the galaxy centre that does not significantly affect our lower redshift (4XMM) sample. One plausible reason for this scenario could be supernova (SN) feedback. SN can create a rarefied and hot environment, and SN winds can expel recycled gas from the galaxy. The core-collapse SN rate should directly trace the SFR (and Type Ia SN rate is small compared to the core-collapse SN; e.g. Dekel et al. 2019). The average SFR among star-forming galaxies in the COSMOS sample is much higher than that among the 4XMM sample (consistent with the fact that galaxies in the COSMOS sample have higher redshift), which is associated with stronger SN feedback. We also note that for $10 < \log M_\star \leq 11$ galaxies in the 4XMM sample, the decline of $\overline{\mathrm{BHAR}/M_\star}$ with $\mathrm{D_n}4000$ among relatively young galaxies

[11]We note that it is also plausible that for the bins we used for scaling calibration with $\mathrm{D_n}4000 \approx 1.9$, the $\overline{\mathrm{BHAR}/M_\star}$ is below the prediction from stellar mass loss rate due to AGN feedback from jets.

Downloaded from https://academic.oup.com/mnras/article/524/3/4778/7224006 by Rijksuniversiteit Groningen user on 26 September 2023

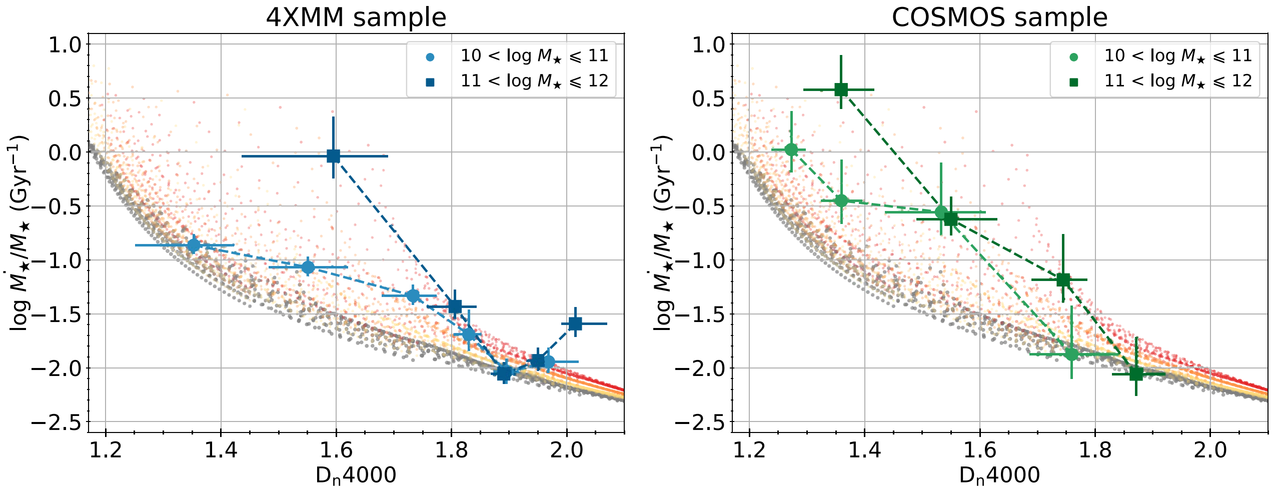

Figure 14. *Left panel:* scaled $\overline{\mathrm{BHAR}/M_\star}$ as a function of D_n4000 among galaxies in 4XMM sample in different $M_\star$ ranges (the scaling factor is selected to align the D_n4000 bin with the lowest $\overline{\mathrm{BHAR}/M_\star}$ value with stellar mass loss rate), plotted against stellar mass loss rate per stellar mass unit per Gyr (grey dots), as well as the average stellar mass loss rate over the past 1 Gyr (yellow dots), 2 Gyrs (orange dots), and 3 Gyrs (red dots). The horizontal position of each data point represents the median D_n4000 of the sources in each bin, with *x*-axis error bars demonstrating the 16th and 84th percentiles of the D_n4000 values in each bin. The *y*-axis error bars represent the 1σ confidence interval of $\overline{\mathrm{BHAR}/M_\star}$ from bootstrapping. *Right panel:* similar to the left panel, but for scaled $\overline{\mathrm{BHAR}/M_\star}$ as a function of D_n4000 among galaxies in the COSMOS sample in different $M_\star$ ranges.

is not as steep as that among $11 < \log M_\star \leq 12$ galaxies, which might also be attributed to SN winds that are more effective at expulsion when the central surface mass density is low (e.g. Hopkins et al. 2022).

4.2 Additional fuelling mechanism and/or enhanced accretion capability among old, massive galaxies in the local universe

We have shown in Fig. 13 that $\overline{\mathrm{BHAR}}$ among the oldest galaxies in the 4XMM sample also does not track the stellar mass loss rate, and appears to be higher than expected from the stellar mass loss fuelling. Among these most massive systems at $D_n4000 \sim 2$, additional fuelling mechanisms (such as the fuelling from hot gas in the halo) may take place, leading to the high $\overline{\mathrm{BHAR}/M_\star}$.[12] The additional fuelling mechanism may also be particularly effective in triggering low-accretion-rate AGNs among old, massive galaxies at low redshift, as can be seen in Fig. 10. Hot halo gas fuelling has long been introduced as a source for powering radio AGNs, particularly LERGs, which tend to have old and massive hosts (e.g. Best & Heckman 2012). In Fig. 12, we can see that the fraction of LERG increases with D_n4000. Also, the LERG population among old galaxies tends to increase with D_n4000 when controlling for $M_\star$, SFR, z (in contrast, the HERG population and the LERG population among young galaxies tend to decrease with D_n4000 when controlling for $M_\star$, SFR, z). It is plausible that the fuelling from the hot halo gas could explain both the increasing fraction of low-accretion-rate X-ray AGN and the increasing fraction of LERG among old galaxies. With this additional fuelling mechanism that is more effective among old galaxies, we also do not observe any sign of a decreasing trend of BH growth associated with D_n4000 among the oldest galaxies in the 4XMM sample in Fig. 7.

It is also plausible that the relatively high $\overline{\mathrm{BHAR}}$ among old galaxies at low redshift is linked with enhanced capability of BH accretion among these galaxies (e.g. Gaspari, Brighenti & Temi 2015; McDonald et al. 2021). Using hydrodynamic simulations, Gaspari et al. (2015) suggest that among massive galaxies, chaotic cold accretion of condensed hot gas is less efficient when a rotating disc is present. Thus, BHs in dispersion-dominated systems might accrete a larger fraction of gas supply than in rotation-dominated systems. As the fraction of elliptical galaxies increases with D_n4000, this might also explain the increasing number of low-accretion-rate AGNs as well as the increasing $\overline{\mathrm{BHAR}}$ with D_n4000 among old, massive galaxies in the 4XMM sample.

5 SUMMARY AND CONCLUSIONS

Utilizing spectroscopic samples of galaxies with X-ray data coverage, we studied the incidence of AGNs among galaxies with different mean stellar population ages in this work. The main points from this paper are the following:

(i) we built two samples of galaxies/AGNs with both spectroscopic coverage and X-ray coverage. One sample (4XMM sample) includes SDSS galaxies with *XMM–Newton* coverage at $z = 0$–0.35; our other sample (COSMOS sample) includes LEGA-C galaxies with *Chandra* coverage at $z = 0.6$–1.0. D_n4000 measurements from spectra are adopted as a tracer of the mean stellar population age of the galaxy. X-ray observations are utilized to estimate AGN fraction and $\overline{\mathrm{BHAR}}$ for samples of galaxies (see Section 2).

(ii) In Section 3.1, we characterized how the AGN fraction, $\overline{\mathrm{BHAR}}$ as well as $\overline{\mathrm{BHAR}/M_\star}$ vary with D_n4000 among galaxies in the 4XMM sample and COSMOS sample. In Section 4.1, we show that $\overline{\mathrm{BHAR}/M_\star}$ as a function of D_n4000 roughly traces the scaled stellar mass loss rate predicted by D_n4000 among galaxies in the 4XMM sample (except for the oldest galaxies) as well as

[12]We note that hot gas among giant ellipticals also shines in the X-ray (e.g. Boroson, Kim & Fabbiano 2011), but the contribution from the diffuse hot gas alone can not account for the excess amount of $\overline{\mathrm{BHAR}}$ observed in the largest D_n4000 bin in the 4XMM sample. For ellipticals with $\log M_\star \sim 11$, we expect diffuse hot emission with $\log L_X \sim 40$. Converting it to $\overline{\mathrm{BHAR}}$, it is at the level of $\log \overline{\mathrm{BHAR}} \sim -5$ and $\log \overline{\mathrm{BHAR}/M_\star} \sim -7\,\mathrm{Gyr}^{-1}$, far below the values we observed.

Downloaded from https://academic.oup.com/mnras/article/524/3/4778/7224006 by Rijksuniversiteit Groningen user on 26 September 2023

old/quiescent galaxies in the COSMOS sample, indicating stellar mass loss as a potentially important (and possibly dominant) fuelling source.

(iii) In Section 3.2, we found that when controlling for host-galaxy properties ($M_\star$, SFR, and z), the fraction of log $L_X/M_\star > 32$ AGNs and $\overline{\rm BHAR}$ decrease with D_n4000 among galaxies in the 4XMM sample (except for the oldest/most massive galaxies) and COSMOS sample, suggesting higher numbers of AGNs and higher levels of BH growth among younger galaxies. We also observed similar trends in terms of the MIR-selected AGN fraction and the HERG fraction among SDSS galaxies in Section 3.4. These results further support the scenario of stellar mass loss as a potential fuelling source for AGN (see Section 4.1).

(iv) In Section 3.1, we observed a slight increase of $\overline{\rm BHAR}$ and $\overline{{\rm BHAR}/M_\star}$ among the oldest galaxies in the local universe; in Section 3.3, we found that among the most massive galaxies in the local universe, the fraction of low specific-accretion-rate AGNs ($31 < \log L_X/M_\star < 32$) increases significantly with D_n4000. The LERG fraction in the local universe also increases with D_n4000 among the old, massive galaxies (see Section 3.4). Additional fuelling from the hot halo gas and potentially enhanced accretion capability among old, massive galaxies may explain these trends (see Section 4.2).

Our work shows that stellar mass loss may be an important fuelling source to trigger AGN activity and thus drive ongoing BH growth, not only among old quiescent galaxies, but also among young star-forming galaxies at low redshift.

ACKNOWLEDGEMENTS

We thank the anonymous referee for constructive feedback. We thank Johan Comparat for the helpful discussion. QN and JA acknowledge support from a UKRI Future Leaders Fellowship (grant code: MR/T020989/1). KLB acknowledges funding from a Horizon 2020 grant (XMM2Athena). For the purpose of open access, the authors have applied a Creative Commons Attribution (CC BY) licence to any author accepted manuscript version arising from this submission.

DATA AVAILABILITY

The data underlying this article were accessed from the *XMM–Newton* Science Archive, SDSS data releases, *Chandra* data archive, and ESO data portal. The derived data generated in this research will be shared upon reasonable request to the corresponding author.

REFERENCES

Adelman-McCarthy J. K., et al., 2011, VizieR Online Data Catalog, II, 306
Aird J., et al., 2010, MNRAS, 401, 2531
Aird J., et al., 2012, ApJ, 746, L90
Aird J., Coil A. L., Georgakakis A., 2017, MNRAS, 465, 3390
Aird J., Coil A. L., Georgakakis A., 2018, MNRAS, 474, 1225
Aird J., Coil A. L., Georgakakis A., 2019, MNRAS, 484, 4360
Aird J., Coil A. L., Kocevski D. D., 2022, MNRAS, 515, 4860
Assef R. J., Stern D., Noirot G., Jun H. D., Cutri R. M., Eisenhardt P. R. M., 2018, ApJS, 234, 23
Balogh M. L., Morris S. L., Yee H. K. C., Carlberg R. G., Ellingson E., 1999, ApJ, 527, L54
Barro G., et al., 2017, ApJ, 840, L47
Best P. N., Heckman T. M., 2012, MNRAS, 421, 1569
Best P. N., Kauffmann G., Heckman T. M., Brinchmann J., Charlot S., Ivezić Ž., White S. D. M., 2005, MNRAS, 362, 25
Birchall K. L., Watson M. G., Aird J., Starling R. L. C., 2022, MNRAS, 510, 4556
Bongiorno A., et al., 2016, A&A, 588, 78
Boquien M., Burgarella D., Roehlly Y., Buat V., Ciesla L., Corre D., Inoue A. K., Salas H., 2019, A&A, 622, 103
Boroson B., Kim D.-W., Fabbiano G., 2011, ApJ, 729, L12
Brandt W. N., Alexander D. M., 2015, A&A Rev., 23, 1
Brandt W. N., Yang G., 2022, Handbook of X-ray and Gamma-ray Astrophysics, p. 78
Brinchmann J., Charlot S., White S. D. M., Tremonti C., Kauffmann G., Heckman T., Brinkmann J., 2004, MNRAS, 351, 1151
Cameron E., 2011, PASA, 28, 128
Chabrier G., 2003, PASP, 115, 763
Chen C. T. J., et al., 2018, MNRAS, 478, 2132
Ciotti L., Ostriker J. P., 2007, ApJ, 665, L1038
Civano F., et al., 2016, ApJ, 819, L62
Conroy C., Gunn J. E., 2010, ApJ, 712, L833
Conroy C., Gunn J. E., White M., 2009, ApJ, 699, L486
de Jong R. S., et al., 2019, The Messenger, 175, 3
DESI Collaboration et al., 2016, preprint (arXiv:1611.00036)
Dekel A., Sarkar K. C., Jiang F., Bournaud F., Krumholz M. R., Ceverino D., Primack J. R., 2019, MNRAS, 488, 4753
Evans I. N., et al., 2010, ApJS, 189, 37
Faber S. M., et al., 2007, ApJ, 665, L265
Fragos T., Lehmer B. D., Naoz S., Zezas A., Basu-Zych A., 2013, ApJ, 776, L31
Gallazzi A., Charlot S., Brinchmann J., White S. D. M., Tremonti C. A., 2005, MNRAS, 362, 41
Gaspari M., Brighenti F., Temi P., 2015, A&A, 579, 62
Georgantopoulos I., Pouliasis E., Mountrichas G., Van der Wel A., Marchesi S., Lanzuisi G., 2023, A&A, 673, 67
Gilbertson W., et al., 2022, ApJ, 926, L28
Hopkins P. F., Hernquist L., 2006, ApJS, 166, 1
Hopkins P. F., Richards G. T., Hernquist L., 2007, ApJ, 654, L731
Hopkins P. F., Wellons S., Anglés-Alcázar D., Faucher-Giguère C.-A., Grudić M. Y., 2022, MNRAS, 510, 630
Ilbert O., et al., 2013, A&A, 556, 55
Kauffmann G., Heckman T. M., 2009, MNRAS, 397, 135
Kauffmann G., et al., 2003, MNRAS, 341, 33
Kocevski D. D., et al., 2017, ApJ, 846, L112
Kormendy J., Ho L. C., 2013, ARA&A, 51, 511
Laigle C., et al., 2016, ApJS, 224, 24
Land K., et al., 2008, MNRAS, 388, 1686
Lehmer B. D., et al., 2016, ApJ, 825, L7
Lintott C. J., et al., 2008, MNRAS, 389, 1179
Luo B., et al., 2017, ApJS, 228, 2
Madau P., Dickinson M., 2014, ARA&A, 52, 415
Magorrian J., et al., 1998, AJ, 115, 2285
Marconi A., Hunt L. K., 2003, ApJ, 589, L21
Marocco F., et al., 2021, ApJS, 253, 8
McConnell N. J., Ma C.-P., 2013, ApJ, 764, L184
McDonald M., McNamara B. R., Calzadilla M. S., Chen C.-T., Gaspari M., Hickox R. C., Kara E., Korchagin I., 2021, ApJ, 908, L85
McLure R. J., et al., 2018, MNRAS, 479, 25
Mountrichas G., et al., 2022, A&A, 667, 145
Ni Q., Yang G., Brandt W. N., Alexander D. M., Chen C. T. J., Luo B., Vito F., Xue Y. Q., 2019, MNRAS, 490, 1135
Ni Q., et al., 2021a, ApJS, 256, 21
Ni Q., et al., 2021b, MNRAS, 500, 4989
Ruiz A., Georgantopoulos I., Corral A., 2021, A&A, 645, 74
Ruiz A., Georgakakis A., Gerakakis S., Saxton R., Kretschmar P., Akylas A., Georgantopoulos I., 2022, MNRAS, 511, 4265
Salim S., et al., 2007, ApJS, 173, 267
Salim S., et al., 2016, ApJS, 227, 2
Salvato M., et al., 2018, MNRAS, 473, 4937
Silverman J. D., et al., 2009, ApJ, 696, L396
Strauss M. A., et al., 2002, AJ, 124, 1810
Toyouchi D., Hosokawa T., Sugimura K., Nakatani R., Kuiper R., 2019, MNRAS, 483, 2031
van der Wel A., et al., 2014, ApJ, 788, L28

Downloaded from https://academic.oup.com/mnras/article/524/3/4778/7224006 by Rijksuniversiteit Groningen user on 26 September 2023

van der Wel A., et al., 2016, ApJS, 223, 29
van der Wel A., et al., 2021, ApJS, 256, 44
Vanden Berk D. E., et al., 2001, AJ, 122, 549
Wang T., et al., 2017, A&A, 601, 63
Webb N. A., et al., 2020, A&A, 641, 136
Wu P.-F., et al., 2018, ApJ, 868, L37
Yang G., Brandt W. N., Darvish B., Chen C. T. J., Vito F., Alexander D. M., Bauer F. E., Trump J. R., 2018, MNRAS, 480, 1022
Yang G., et al., 2020, MNRAS, 491, 740

APPENDIX A: ASSESSING THE RELIABILITY OF D_n4000 MEASUREMENTS FOR AGNS

As we limit our sample to objects with galaxy-like spectra in this study (i.e. quasar-like sources with prominent broad emission lines are excluded), X-ray AGNs in our sample are type 2 AGNs with obscured disc emission. Thus, the AGN power-law continuum should have little contribution to the optical spectra. However, it is possible for a galaxy to look younger in the spectrum when an AGN component (even if the contribution is small) is present, as quasars have a bluer continuum compared to galaxies. In this appendix, we assess whether the AGN disc emission affects the reliability of D_n4000 measurements for AGNs in our sample.

In Fig. A1, we present the composite spectra of galaxies/AGNs in the 4XMM sample in different D_n4000 bins ($D_n4000 = 1.1$–2.0 with a step of 0.1 and a bin size of 0.1), with the composite quasar spectrum from Vanden Berk et al. (2001) shown as well. In Fig. A2, we present the composite spectra of galaxies/AGNs in the COSMOS sample in different D_n4000 bins ($D_n4000 = 1.3$–1.7 with a step of 0.1 and a bin size of 0.1). Here, AGNs are defined as objects with $\log L_X/M_\star > 31$. Galaxies are defined as objects not detected in the X-ray. The composite spectra are created by normalizing each individual spectrum in the subsample at rest-frame 4050 Å, and taking the median value. The presented composite spectra are smoothed with a boxcar with a width of 10 Å. We can see that the composite spectra of AGN look generally similar to those of galaxies, and do not exhibit signs of any broad line. In Figs A3 and A4, we present the 4XMM sample AGN and galaxy composite spectra in different D_n4000 bins in different panels; in each panel, we

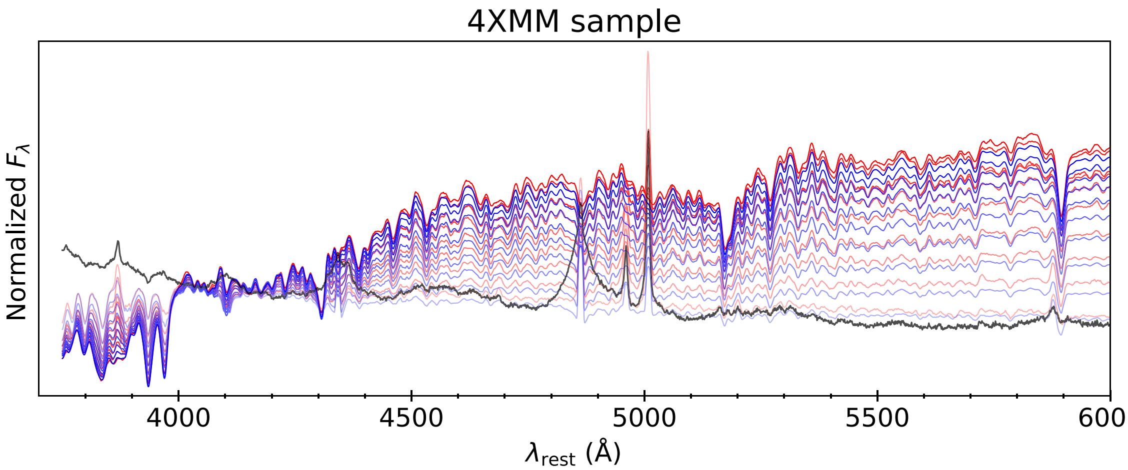

Figure A1. Normalized composite spectra of galaxies or AGNs in different D_n4000 bins ($D_n4000 = 1.1$–2.0 with a step of 0.1 and a bin size of 0.1) for the 4XMM sample, represented by the blue or red lines; the deeper the colour, the larger the D_n4000 value. The SDSS quasar composite spectrum from Vanden Berk et al. (2001) is shown as the black line for comparison.

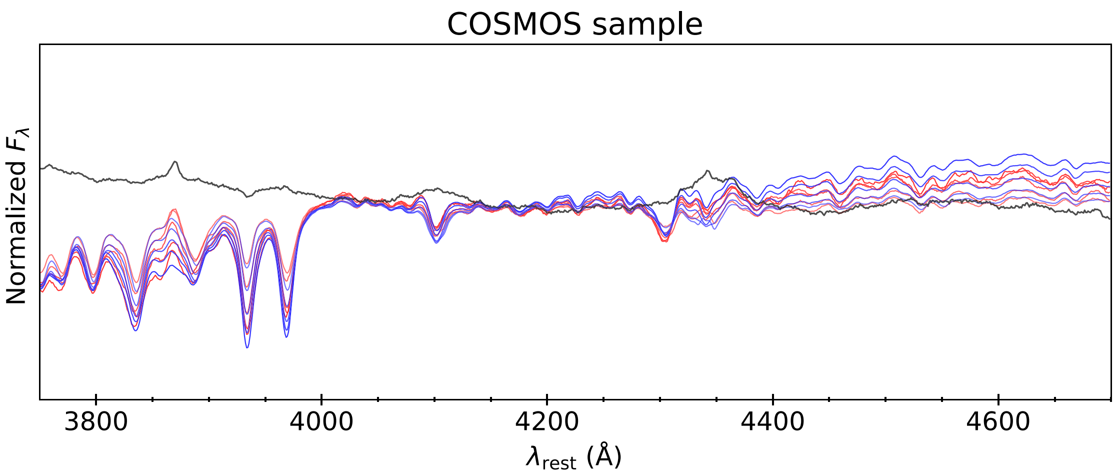

Figure A2. Similar to Fig. A1, but for galaxies or AGNs in different D_n4000 bins ($D_n4000 = 1.3$–1.7 with a step of 0.1 and a bin size of 0.1) in the COSMOS sample.

Downloaded from https://academic.oup.com/mnras/article/524/3/4778/7224006 by Rijksuniversiteit Groningen user on 26 September 2023

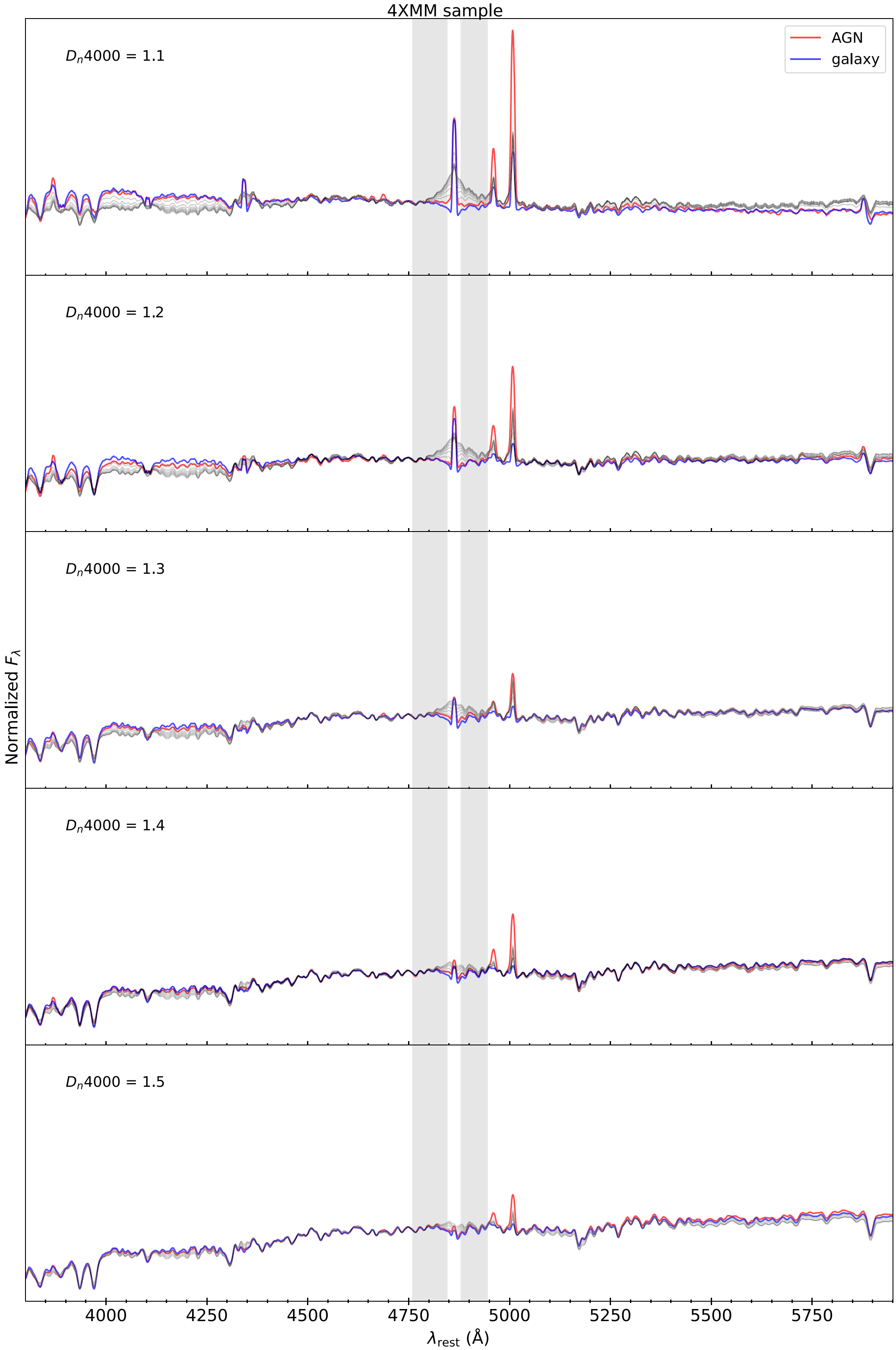

Figure A3. In each panel, normalized composite spectra of galaxies or AGNs in the 4XMM sample at a given D_n4000 bin (with a median D_n4000 value as labelled) are represented by the blue or red lines; the black lines represent synthetic spectra created by combining galaxy composite spectra that have stronger D_n4000 with the Vanden Berk et al. (2001) composite quasar spectrum in a proportion that mimics the *observed* D_n4000 of the presented AGN composite spectrum. These synthetic spectra show excess emission around the broad Hβ wings (indicated by the grey regions) compared to galaxy composite spectra. We estimate the possible bias in the D_n4000 measurements for AGNs in our sample by choosing the synthetic combination that best matches the observed excess flux of the AGN composite spectrum over the galaxy composite spectrum in the grey regions. All the spectra presented are normalized at 4750 Å.

Downloaded from https://academic.oup.com/mnras/article/524/3/4778/7224006 by Rijksuniversiteit Groningen user on 26 September 2023

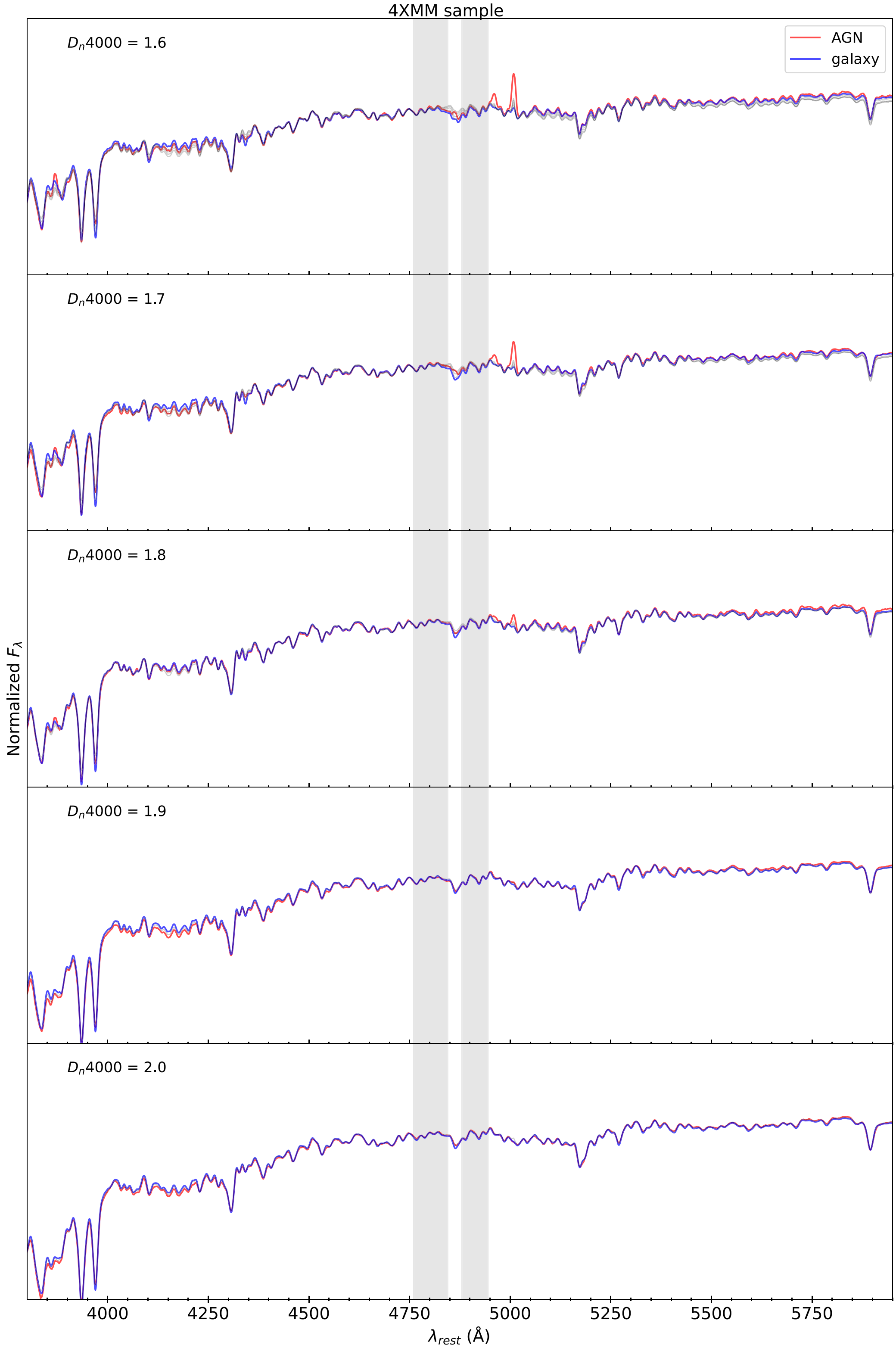

Figure A4. Fig. A3 continued.

also present spectra constituted by the composite galaxy spectrum from bins with larger D_n4000 values and the Vanden Berk et al. (2001) quasar spectrum, but can mimic the D_n4000 value of this panel. We can see that including the quasar emission will lead to a small bump around the Hβ line region, which is not obvious among AGN composite spectra in our sample. We also perform the same procedures for the AGN and galaxy composite spectra in the COSMOS sample, and the results are presented in Fig. A5.

Downloaded from https://academic.oup.com/mnras/article/524/3/4778/7224006 by Rijksuniversiteit Groningen user on 26 September 2023

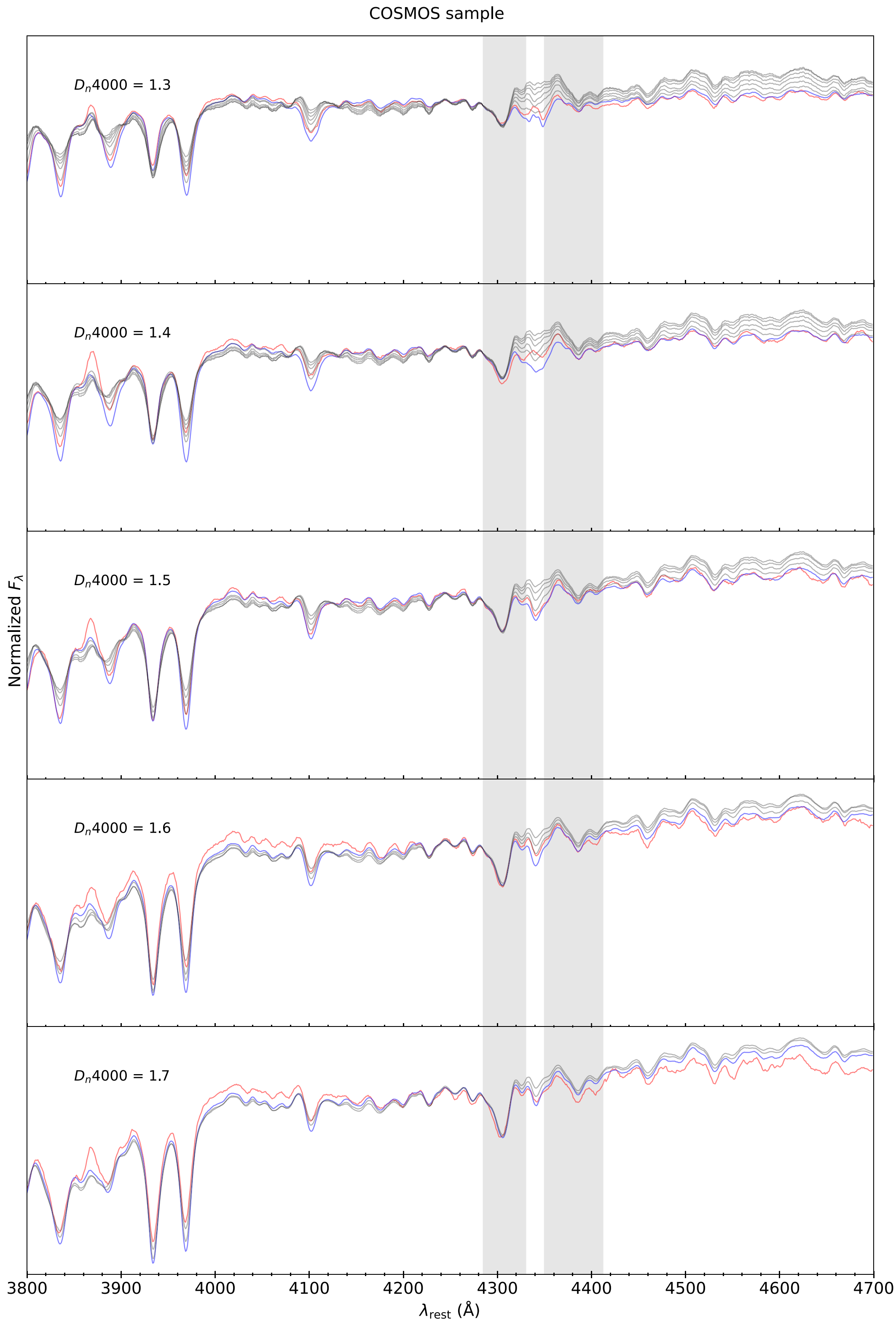

Figure A5. Similar to Fig. A3, but for galaxies or AGNs in the COSMOS sample. The synthetic spectra represented by black lines show excess emission around the broad Hγ wings (indicated by the grey regions) compared to galaxy composite spectra. All the spectra presented are normalized at 4285 Å.

Including the quasar emission will make the bump around the Hγ line region noticeable in the spectra, which is not obvious among our AGN composite spectra. The lack of apparent differences in the broad emission-line regions of our AGN composite spectra compared to galaxy composite spectra indicates that severe contamination is unlikely.

To quantify the bias in D_n4000 measurements of AGNs related to 'hidden' AGN emission, we utilize the ratio of the integrated

Downloaded from https://academic.oup.com/mnras/article/524/3/4778/7224006 by Rijksuniversiteit Groningen user on 26 September 2023

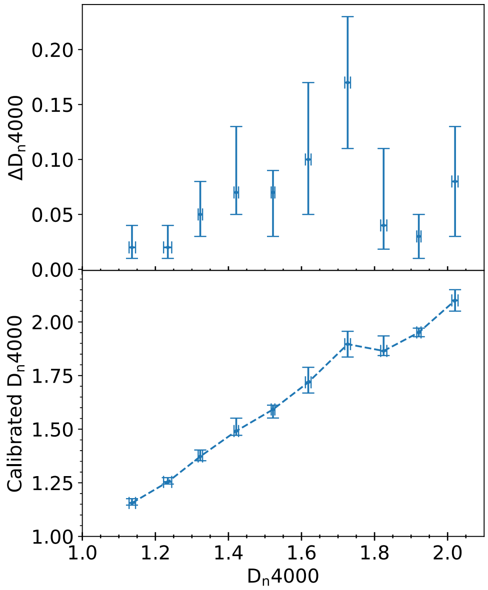

Figure A6. *Top:* the underestimation of D_n4000 (due to contamination from underlying AGN emission) versus observed D_n4000 of AGNs in the 4XMM sample, with error bars representing the 1σ confidence intervals obtained from bootstrapping. *Bottom:* 'Calibrated' D_n4000 values (when accounting for the bias) versus D_n4000 values reported when assuming no AGN component for AGNs in the 4XMM sample. We have verified that our results do not change qualitatively when utilizing these 'calibrated' D_n4000 values for AGNs.

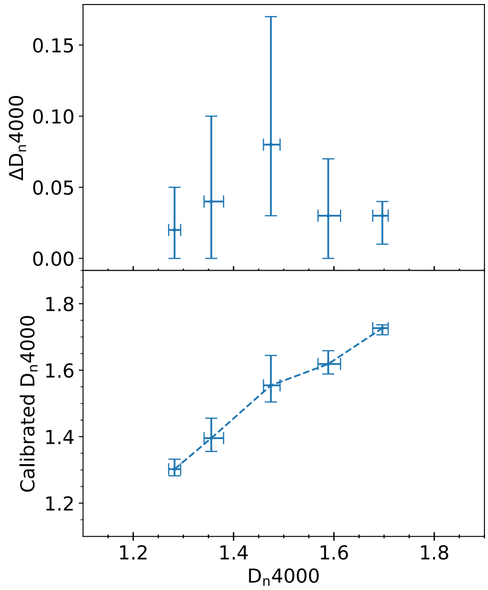

Figure A7. Similar to Fig. A6, but for AGNs in the COSMOS sample.

flux in the shaded regions presented in Figs A3, A4, or A5 between the composite AGN spectrum and galaxy spectrum; these regions characterize the broad Hβ wings for SDSS spectra and the broad Hγ wings for LEGA-C spectra. We create galaxy composite spectra in the D_n4000 grid with a step of 0.01, and mix the galaxy spectra with quasar template to make the D_n4000 value equal to that of the AGN composite spectrum in the given D_n4000 bin. For a given D_n4000 bin, when the ratio of the integrated flux in the shaded regions between the synthetic quasar plus galaxy spectrum and the composite galaxy spectrum is close to that between the composite AGN spectrum and the composite galaxy spectrum, we think D_n4000 of the galaxy component in the synthetic spectrum represents the true D_n4000 of the AGN composite spectrum, so that the bias can be estimated. The uncertainty of the bias could be obtained by bootstrapping AGNs in different D_n4000 bins, creating different composite AGN spectra, and repeating the earlier procedures. The results are presented in Fig. A6 for the 4XMM sample and Fig. A7 for the COSMOS sample. We can see that the bias is generally small ($\lesssim 0.1$–0.2), and 'calibrating' the measured D_n4000 values of AGNs with bias will not change the general D_n4000 trend. We have also verified that our results do not change qualitatively when utilizing 'calibrated' D_n4000 values (i.e. the measured values plus the bias estimated from the earlier method) for AGNs.

APPENDIX B: THE PROBABILITY DENSITY DISTRIBUTION OF A GALAXY HOSTING AN AGN AS A FUNCTION OF $L_X/M_\star$ IN THE 4XMM SAMPLE

We note that, in Section 3.1, the AGN fraction is defined as a single fraction with $L_X/M_\star$ greater than a given value, which we take to be 10^{32}. To test whether this arbitrary threshold will affect our results, we further model the probability of finding an AGN as a function of $L_X/M_\star$ in the 4XMM sample for all the bins in Fig. 5. For the COSMOS sample, this type of analysis is limited by the small number of AGNs detected in each bin. We could see that this probability density distribution of a galaxy hosting an AGN as a function of $L_X/M_\star$ as shown in Fig. B1 follows a rough linear relation in the log-log space, similar to what has been found by Birchall et al. (2022). Thus, the $L_X/M_\star$ threshold adopted when calculating the AGN fraction would not materially affect the results.

Downloaded from https://academic.oup.com/mnras/article/524/3/4778/7224006 by Rijksuniversiteit Groningen user on 26 September 2023

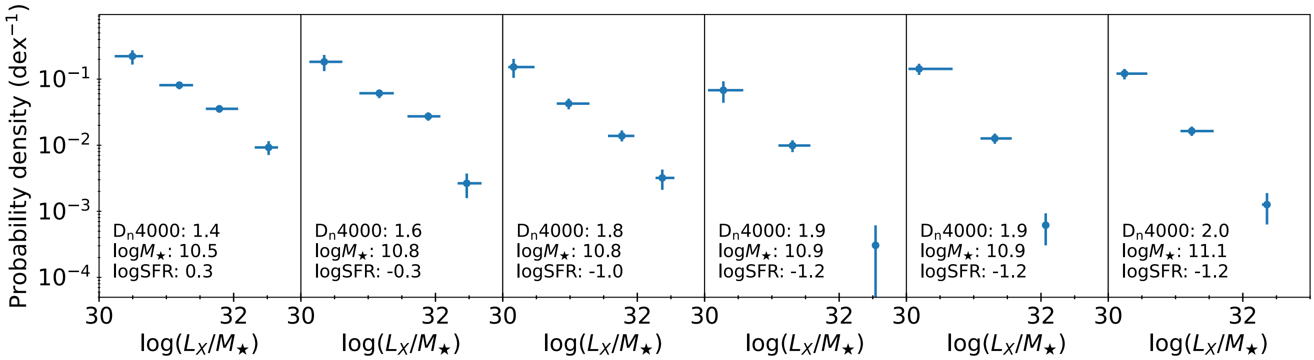

Figure B1. Distributions showing the probability of finding an AGN as a function of specific BH accretion rate. Different panels have different D$_n$4000.

APPENDIX C: AGN FRACTION (DEFINED WITH L_X) AS A FUNCTION OF D$_n$4000 WHEN CONTROLLING FOR $M_\star$, SFR, AND z

In Section 3.2, we examined how the fraction of log $L_X/M_\star > 32$ AGN changes with D$_n$4000 when controlling for $M_\star$, SFR, and z. In Fig. C1/C2, we present how the fraction of log $L_X > 42$ AGN (in the case, AGNs are defined with luminosity rather than with 'specific BH accretion rate') changes with D$_n$4000 when controlling for $M_\star$, SFR, and z for the 4XMM/COSMOS sample. We could see that similar to the trends we observed in Figs 7 and 8, the log $L_X > 42$ AGN fraction displays a consistent decreasing trend with D$_n$4000 among galaxies in the 4XMM sample (except for the oldest galaxies) and the COSMOS sample.

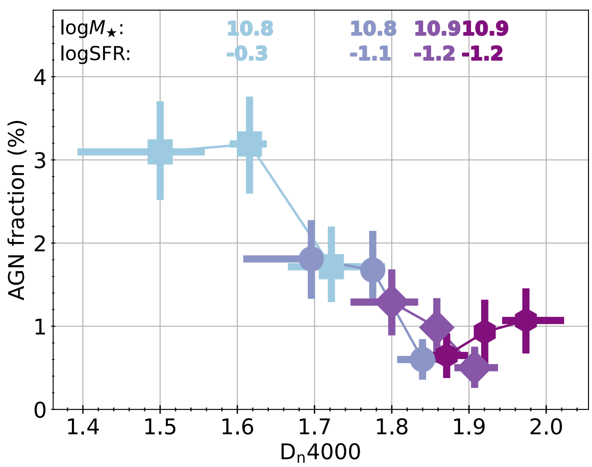

Figure C1. AGN fraction (defined by log $L_X > 42$) as a function of D$_n$4000 among galaxies in the 4XMM sample when controlling for $M_\star$, SFR, and z. Different symbols and colours represent a set of subsamples with similar $M_\star$, SFR, and z values (as listed on top of the panel with the same colour). The horizontal position of each data point represents the median D$_n$4000 of the sources in each sample, with x-axis error bars demonstrating the 16th and 84th percentiles of the D$_n$4000 values. The y-axis error bars represent the 1σ confidence interval of AGN fraction from bootstrapping.

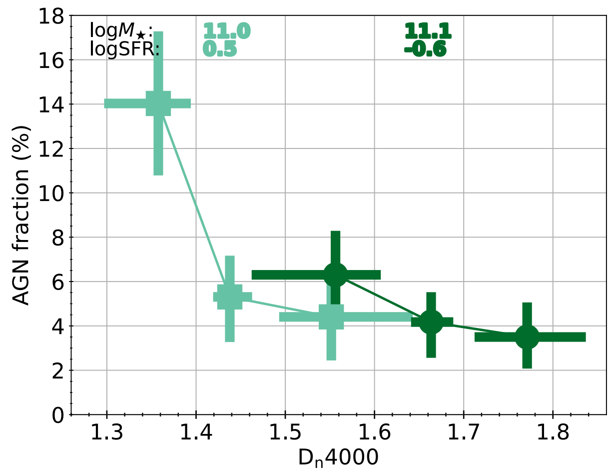

Figure C2. Similar to Fig. C1, but for AGN fraction as a function of D$_n$4000 among galaxies in the COSMOS sample.

APPENDIX D: AGN FRACTION AS A FUNCTION OF D$_n$4000 WHEN CONTROLLING FOR MORPHOLOGY

We also tested whether host-galaxy morphology has an influence on the observed trends with D$_n$4000, as the dominant galaxy morphological type changes with the age of galaxies, and it is plausible that different morphological types have different BH fuelling patterns. For the 4XMM sample, we perform the elliptical/spiral morphological classification with the Galaxy Zoo data (Lintott et al. 2008), utilizing the CLEAN criterion developed by Land et al. (2008). For elliptical galaxies, we can see that the AGN fraction/$\overline{\mathrm{BHAR}}$ does not decrease significantly with D$_n$4000 at D$_n$4000 $\sim$ 1.8–2.0 when controlling for $M_\star$, SFR, and z in Fig. D1, similar to what we observed in Fig. 7. For spiral galaxies, there is a clear trend that the AGN fraction/$\overline{\mathrm{BHAR}}$ drops with D$_n$4000 (see Fig. D2). For the COSMOS sample, we adopt the bulge-dominated (BD) and non-bulge-dominated (non-BD) morphological classification from Ni et al. (2021b) and perform the same analyses for BD galaxies and non-BD galaxies separately. We note that, among 449 BD galaxies

Downloaded from https://academic.oup.com/mnras/article/524/3/4778/7224006 by Rijksuniversiteit Groningen user on 26 September 2023

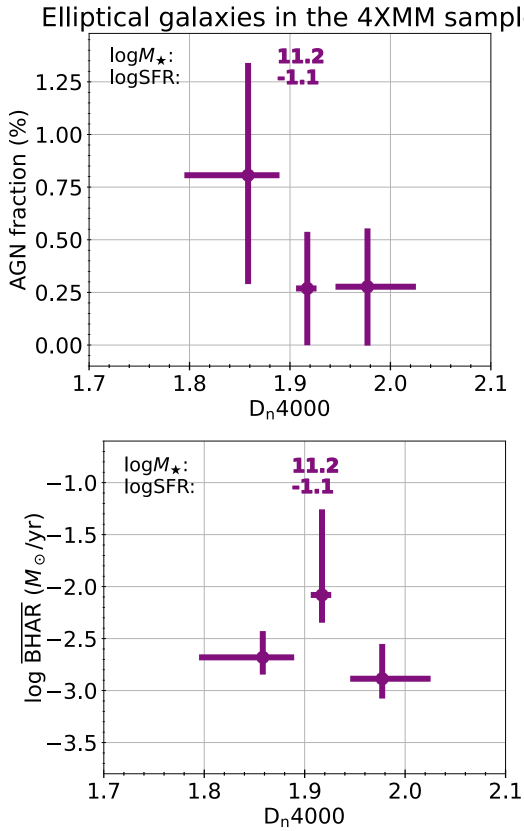

Figure D1. *Top:* AGN fraction as a function of D_n4000 among elliptical galaxies in the 4XMM sample when controlling for $M_\star$, SFR, and z. All the subsamples share similar $M_\star$, SFR, and z values. The horizontal position of each data point represents the median D_n4000 of the sources in each subsample, with x-axis error bars demonstrating the 16th and 84th percentiles of the D_n4000 values. The y-axis error bars represent the 1σ confidence interval of AGN fraction from bootstrapping. *Bottom:* $\overline{\mathrm{BHAR}}$ as a function of D_n4000 among elliptical galaxies in the 4XMM sample when controlling for $M_\star$, SFR, and z. All the subsamples share similar $M_\star$, SFR, and z values. The horizontal position of each data point represents the median D_n4000 of the sources in each subsample, with x-axis error bars demonstrating the 16th and 84th percentiles of the D_n4000 values. The y-axis error bars represent the 1σ confidence interval of $\overline{\mathrm{BHAR}}$ from bootstrapping.

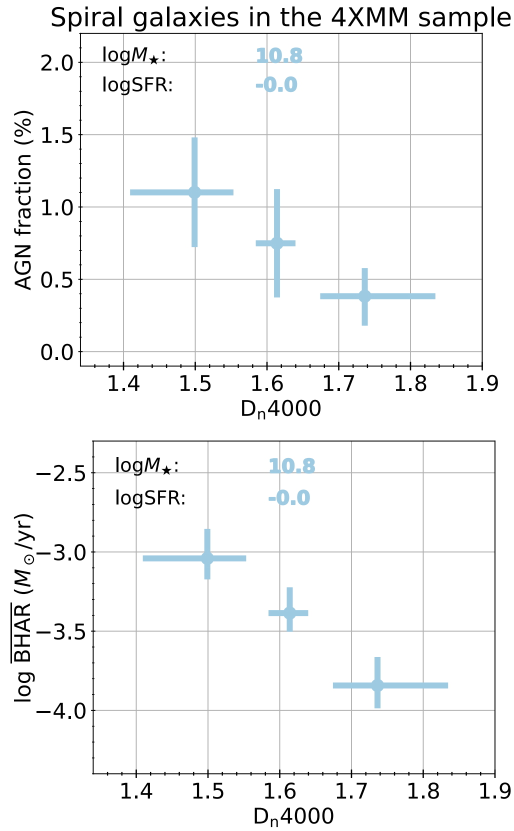

Figure D2. *Top:* similar to the top panel of Fig. D1, but for spiral galaxies in the 4XMM sample. *Bottom:* similar to the bottom panel of Fig. D1, but for spiral galaxies in the 4XMM sample.

in the COSMOS sample, only 7 of these galaxies have log $L_X/M_\star$ >32. Thus, for the analyses here, we do not adopt the stringent $L_X/M_\star$ threshold as we did for the previous analyses. We directly adopt the fraction of objects with log $L_X > 42$ as the AGN fraction (without any sensitivity correction), and the results could be seen in Fig. D3. How $\overline{\mathrm{BHAR}}$ varies with D_n4000 when controlling for $M_\star$, SFR, and z is also presented. The results for the non-BD galaxies could be seen in Fig. D4. We can see that a decreasing trend of AGN fraction and $\overline{\mathrm{BHAR}}$ is present (though not very significant) among BD galaxies and non-BD galaxies separately. These results suggest that the observed variation in AGN activity/BH growth with D_n4000 is unlikely due to pure morphological effects.

We also note that host-galaxy structural properties are unlikely to cause the difference in AGN fraction/$\overline{\mathrm{BHAR}}$ associated with D_n4000 observed in our samples. In Ni et al. (2021b), it has been found that BH growth is closely related to host-galaxy compactness (represented by the projected mass density of the central 1 kpc, Σ_1) among star-forming galaxies; higher Σ_1 values are associated with higher levels of AGN activity/BH growth. As older galaxies tend to be more compact, the higher level of AGN activity/BH growth among younger galaxies is unlikely a result of varying structural properties.

Downloaded from https://academic.oup.com/mnras/article/524/3/4778/7224006 by Rijksuniversiteit Groningen user on 26 September 2023

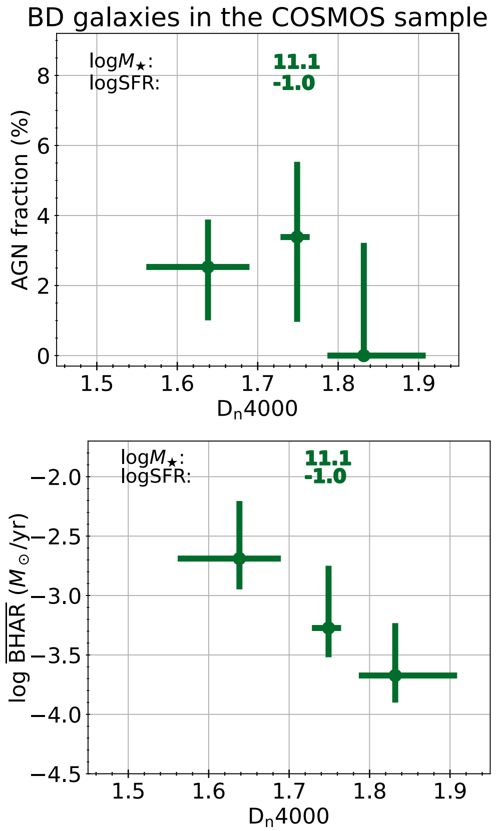

Figure D3. *Top:* similar to the top panel of Fig. D1, but for BD galaxies in the COSMOS sample. *Bottom:* similar to the bottom panel of Fig. D1, but for BD galaxies in the COSMOS sample.

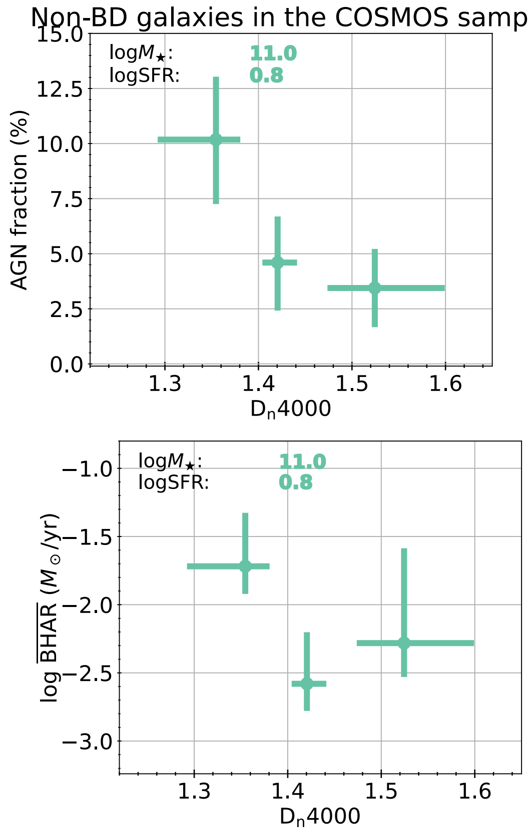

Figure D4. *Top:* similar to the top panel of Fig. D1, but for non-BD galaxies in the COSMOS sample. *Bottom:* similar to the bottom panel of Fig. D1, but for non-BD galaxies in the COSMOS sample.

This paper has been typeset from a TEX/LATEX file prepared by the author.

Downloaded from https://academic.oup.com/mnras/article/524/3/4778/7224006 by Rijksuniversiteit Groningen user on 26 September 2023

© 2023 The Author(s)
Published by Oxford University Press on behalf of Royal Astronomical Society